2

DOE/PC/91155--T5

J-1
2

Coal-Fired High Performance Power Generating System

DE-AC22-92PC91155

Quarterly Progress Report

for the Period July 1 – September 30, 1993

Prepared for

Pittsburgh Energy Technology Center
Pittsburgh, Pennsylvania

United Technologies Research Center
411 Silver Lane, East Hartford, Connecticut 06108

Coal-Fired High Performance Power Generating System

DE-AC22-92PC91155

Quarterly Progress Report

for the Period July 1 – September 30, 1993

Prepared for

Pittsburgh Energy Technology Center
Pittsburgh, Pennsylvania

United Technologies Research Center
411 Silver Lane, East Hartford, Connecticut 06108

DISCLAIMER

CONTENTS

Section	Page
EXECUTIVE SUMMARY	V
CYCLE ANALYSIS	1
CHEMICAL REACTOR MODELING	5
Process Simulation	5
Staging/Reburning	6
Vitiated Air	8
NO Formation in Coal Flames	10
Ignition Effects	14
Modeling the Ignition Front	14
ASH DEPOSITION RATE CALCULATIONS FOR HITAF CONVECTIVE AIR HEATER	18
AIR HEATER MATERIALS	25
DEPOSIT INITIATION AND GROWTH ON CERAMIC SURFACES	32
Refractory Experiments	32
Ceramic Sting Tests – Results for the Experimental DIMOX at 1260°C	37
Experimental	37
Results	38
Conclusions	41
Slag Additives – Copper Oxide	43
REFERENCES	45

TABLES

Table		Page
1.	Steam Enthalpies	2
2.	Ash Particle Size Distribution at Inlet of HITAF Convective Air Heater	21
3.	Geometry And Flow Conditions	21
4.	ALFA IV Typical Composition	26
5.	XRF Analyses for Ashes Used in Corrosion Experiments	37

FIGURES

Figure		Page
1.	Coal-fired HITAF HAT cycle.	1
2.	Coal–Fired HITAF HAT Cycle with Steam Topping.	4
3.	Centerline gas temperature measured in the "U" furnace at two different firing rates.	5
4.	The effect of primary zone residence time on NO emissions in the "U" furnace. Firing rate was 130,000 Btu/hr with an overall stoichiometry of 1.15.	6
5.	Comparison of NO reduction by staging and staging/reburning. Firing rate was 121,000 Btu/hr.	7
6.	Impact of the degree of vitiation on NO emissions in the "U" furnace. Primary zone stoichiometry was 1.05, overall stoichiometry was 1.15.	8
7.	Adiabatic flame temperatures for a bituminous coal burned with "normal" combustion air (21% O2 – 600°F preheat) and "vitiated" combustion air (17.6% O2 – 1010°F preheat).	9
8.	Comparison of high-temperature vitiated combustion air and standard combustion air under staged conditions.	10
9.	Model predictions comparing high-temperature vitiated combustion air (1010°F) and standard combustion air (650°F).	11
10.	Pathways for NO formation in a pulverized coal flame.	12
11.	The influence of mixing conditions on fuel nitrogen conversion.	13
12.	Comparison of measured and predicted centerline temperatures for the attached long axial flame (A1) in the 7 million Btu/hr IFRF furnace.	15
13.	Comparison of measured and predicted centerline temperatures for the unattached long axial flame (B1) in the 7 million Btu/hr IFRF furnace.	16
14.	Gas and particle temperatures along the centerline (in meters) of the 7 million Btu/hr long axial flame of the IFRF furnace tests. Different particle sizes are shown with the corresponding weight percent representing that particle size. The lower temperature (where distinguishable) corresponds to the particle temperature.	17
15.	Convective air heater. Configuration/dimension.	18
16.	Convective air heater, in-line tube array.	19
17.	Convective air heater, staggered tube array.	19
18.	In-line tube array – 5:1 aspect ratio ellipsoidal tubes.	20
19.	Staggered tube array – 5:1 aspect ratio ellipsoidal tubes. tubes.	20
20.	HX3-3 inline circular tubes.	22
21.	HX6-3 inline circular tubes.	23
22.	Growth rates of oxides.	27
23.	Sheet materials – yield strength (0.2% offset).	28
24.	Sheet materials – ultimate tensile strength.	29
25.	Sheet materials – tensile elongation.	30

Figure		Page
26.	Physical properties.	31
27.	Cross section of a cup made of commercially available monolithic SiC refractory filled with ash from a Powder River Basin coal and reacted at 1450°C for 80 hours.	33
28.	Cross section of a refractory cup made from SiC granules and an experimental binder designed for high-calcium slags. The cup was filled with Powder River Basin coal slag and reacted at 1380°C for 80 hours.	33
29.	Cross section of experimental refractory cup made from SiC and an experimental binder designed for low-calcium slags. The cup was filled with Illinois No. 6 coal slag and reacted at 1450°C for 80 hours.	35
30.	The penetration rates of Illinois No. 6 coal slag for the best type of commercial refractory and refractories with 5%, 7.5%, and 10% experimental binder.	35
31.	The temperature-dependent conductivity of experimental SiC-based monolithic refractory made with 15% binder.	36
32.	Illustration of the composite sample embedded in a refractory boat. The refractory boat design allowed containment of the slag during the exposure and prevented interaction of the base of the composite with the slag or refractory.	38
33.	SEM backscatter electron image of a cross section through the composite showing anorthitelike crystals in the slag and a dark alumina scale present at the slag-ceramic interface.	39
34.	X-ray map of Figure 28 showing a layer rich in Al at the slag-ceramic interface, and a layer rich in Si and Al, composed of anorthitelike crystals, on the alumina scale.	40
35.	SEM photo showing porosity development on the surface of the composite. The pores are black and concentrated along the slag-composite interface in the center of the photo.	40
36.	SEM photo of a cross section through the composite showing the dark alumina scale and the overlying, lighter layer of mullite crystals above the slag-ceramic interface. The mullite layer is coated with small, bright crystals of almandine.	42
37.	X-ray map of Figure 31 showing the concentration of Al, Si, Fe, and O2 in the mullite reaction layer at the slag-ceramic interface.	42
38.	SEM photo showing iron oxide crystals that formed in the Illinois No. 6 slag with a 1 wt% copper oxide addition.	44

EXECUTIVE SUMMARY

This report covers work carried out under Task 3, Preliminary R and D, and Task 4, Commercial Generating Plant Design, under contract DE-AC22-92PC91155, "Engineering Development of a Coal Fired High Performance Power Generation System" between DOE Pittsburgh Energy Technology Center and United Technologies Research Center.

The goals of the program are to develop a coal-fired high performance power generation system (HIPPS) by the year 2000 that is capable of

- >47% thermal efficiency
- NO_x, SO_x, and particulates $\leq$25% NSPS
- cost $\geq$ 65% of heat input
- all solid wastes benign

In order to achieve these goals our team has outlined a research plan based on an optimized analysis of a 250 MW_e combined cycle system applicable to both frame type and aeroderivative gas turbines. Under the constraints of the cycle analysis we have designed a high temperature advanced furnace (HITAF) which integrates several combustor and air heater designs with appropriate ash management and procedures.

Recent efforts in cycle optimization have identified a system configuration for the FT-4000 HAT cycle that results in a 48% thermal efficiency. Because of the large number of options in the design, parametric variations will continue until an optimized system is achieved.

Experimental combustor studies have produced new data on NO_x control by primary air staging, natural gas reburn and the use of vitiated air. In the parallel modeling effort, an important achievement has been made in the benchmarking of the 2D code (Jasper) for large scale long axial flames. Using data from the IFRF 7 MBTU/hr furnace, the code has accurately modeled standoff (ignition) distances for conditions comparable to the HITAF.

CFD analysis of the convective air heater indicates that the particle trajectories are similar to those anticipated in the design. The calculations indicate that most of the ash will deposit on the leading edge (or first stage) of the air heater.

Information on a new superalloy, ALFA IV, indicates that it is suitable for both the convective and radiative air heaters when the system operates with 35% natural gas. Further efforts will be made to improve the high temperature strength of this material.

The radiative air heater must be protected by a ceramic refractory coating. Recently, a new experimental refractory based on SiC but with a different binder has shown promise for enhanced resistance to corrosion by low Ca slags.

CYCLE ANALYSIS

The effort in cycle analysis centered on the integration of the Humid Air Turbine (HAT) cycle to the HITAF. Other effort was expended in reviewing the plant layout and balance of plant requirements.

The HAT cycle is a regenerative gas turbine cycle that uses waste heat to humidify compressor discharge air (Figure 1). The resultant air/water vapor mixture is first heated by regeneration with the gas turbine exhaust stream and then further heated in the combustor prior to being expanded. Because of the water vapor, the mass flow and thus the gas turbine output are greatly enhanced. The additional mass flow that produces the increased power is achieved without a corresponding increase in compressor power. Cycle efficiencies approaching 55% on natural gas (LHV) can be achieved at combustor outlet temperatures of 2500°F, using a high pressure ratio aeroderivative gas turbine. In essence, the HAT cycle improves the performance benefits of a combined cycle while eliminating the steam turbine.

In Figure 1, it can be seen that the gas turbine cycle uses intercooling as well as regeneration. The heat from the intercooler, in addition to the low temperature (less than 500°F) exhaust heat and heat from an aftercooler in the high pressure compressor discharge stream, is used in a saturator tower to humidify the compressor exit air to a dew point of approximately 350°F. The amount of exhaust or waste heat utilized is quite high because the dew point out of the gas turbine compressor is on the order of 170°F which allows the tower bottoms temperature to approach 200°F and permits utilization of heat down to that temperature.

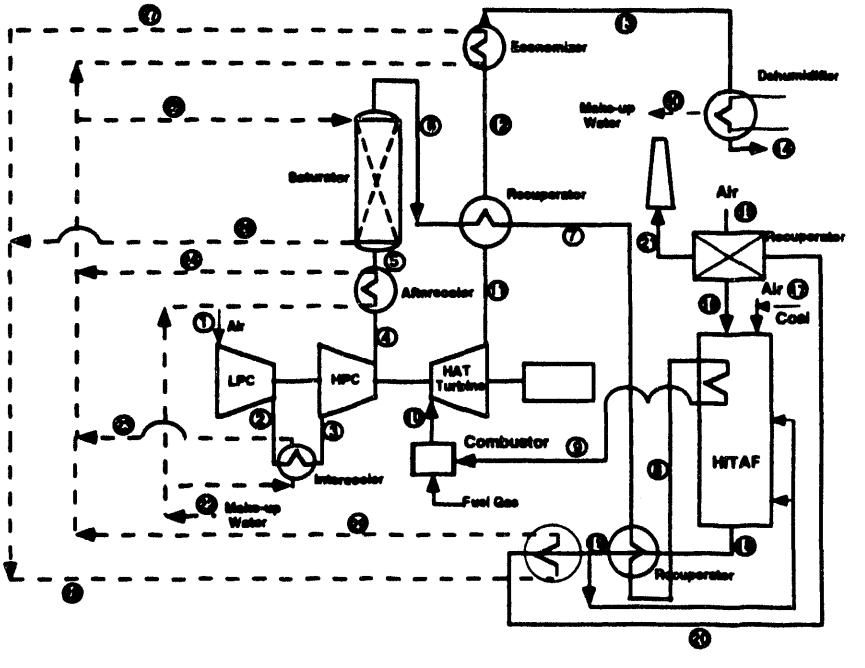

Figure 1. Coal-fired HITAF HAT cycle.

A regenerator takes the place of the combined cycle HRSG to heat the mixture of air and water vapor. Because the water has been vaporized at low temperature, the regenerator effectively superheats the vapor while reheating or regenerating the high pressure air. The mixture is then heated to turbine inlet temperature by a conventional gas turbine burner in the natural gas version, or in a specially designed duct burner in the HITAF application..

The resultant cycle differs from the combined cycle in that there is no "topping" or "bottoming" cycle. The conventional steam cycle is replaced by one having a lower pressure ratio but higher turbine inlet temperature. Water vapor pressure is approximately 135 psia and expands to 4 psia. By virtue of the fact that the air and water vapor streams are combined, the steam cycle also is a regenerative cycle.

While the air and water vapor parts of the cycle cannot be physically separated, it is possible to evaluate the approximate water vapor efficiency and compare it with that of a conventional condensing steam cycle. The steam table enthalpies at the various points of the cycle are presented in Table 1.

Table 1. Steam Enthalpies

	H – Btu/lb	Temp–°F
Feedwater	49	81
Saturator outlet	1214	347
Turbine inlet	2432	2540
Turbine outlet	1449	860
Regenerator outlet	1286	500
Water heater outlet	1165	240

When the water vapor content of the bleed or turbine cooling flow is included, the apparent steam cycle efficiency is approximately 44.4%. (A humidified stream is used to cool the first stage vane of the turbine.) This compares quite favorably with a 2400 psi/1000F /1000°F reheat cycle which would have a thermal efficiency of approximately 40% without regenerative feed water heaters.

The obvious advantages of the HAT cycle are elimination of the steam equipment and improved performance. The improved performance results from better use of low temperature heat along with a more efficient steam cycle. The better use of low temperature heat is evidenced by the fact that the water vaporization process occurs at temperatures below 350°F; whereas a conventional steam bottoming cycle requires a minimum temperature on the order of 650°F to provide the heat of vaporization to the boiler.

The factors that affect the integration of the HAT cycle are quite different than those of the conventional combined cycle. The large amount of water vapor in the gas turbine exhaust (which is

recovered and reused) precludes the use of that stream as the source of primary air for the coal combustion. Therefore, schematically, the HITAF looks like a conventional coal–fired plant complete with an exhaust gas recuperator to heat inlet combustion air.

Ideally, the cycle would not require any steam be raised. However, the need for a slag screen and cooled water wall in the HITAF make it necessary that some steam be raised. With this in mind, candidate systems were proposed and preliminary calculations made to estimate their efficiency.

Four basic approaches were considered:

1) A conventional reheat steam cycle using extraction feed heating to maintain efficiency. The extraction feed heating is needed since there would be little or no low temperature heat available for that use. The resultant steam cycle produced only 25MW. It was concluded that a regenerative steam system of this size would be too small to be economically attractive.

2) Chemical recuperation or reformation of a steam/methane feed using HITAF heat was considered but set aside because of the complexity it would entail to treat only a small portion (natural gas fraction)of the fuel feed.

3) The use of a back pressure steam turbine. In this system, steam raised in the HITAF is expanded in a back pressure turbine prior to injection into the humidified compressor discharge stream. This system is shown schematically in Figure 2. Initial estimates of performance showed efficiency of 47.5% (HHV). It is expected that this can be improved with further efforts at integration. These efforts would be directed primarily at reducing the amount of heat from the HITAF to be used in raising steam.

4) A derivative of the above system would eliminate the back pressure turbine and use the available heat directly in the saturator. This cycle loses the benefit of the steam turbine output but eliminates the turbine and equipment associated with raising and superheating the steam. This appears to be desirable as long as the amount of heat that must be used for raising steam or water vapor is kept to a minimum.

A further variation of the HITAF/HAT cycle was investigated. The effect of increasing the natural gas fraction to allow turbine inlet temperature to increase by 300°F was found to produce an overall system efficiency of 51% (HHV). This turbine inlet value is comparable for those predicted for the next generation of aeroderivative engines.

Because of the sensitivity of the cycle efficiency to effective use of low grade heat, a number of minor variations in HITAF configuration will be investigated to identify the best overall integrated system.

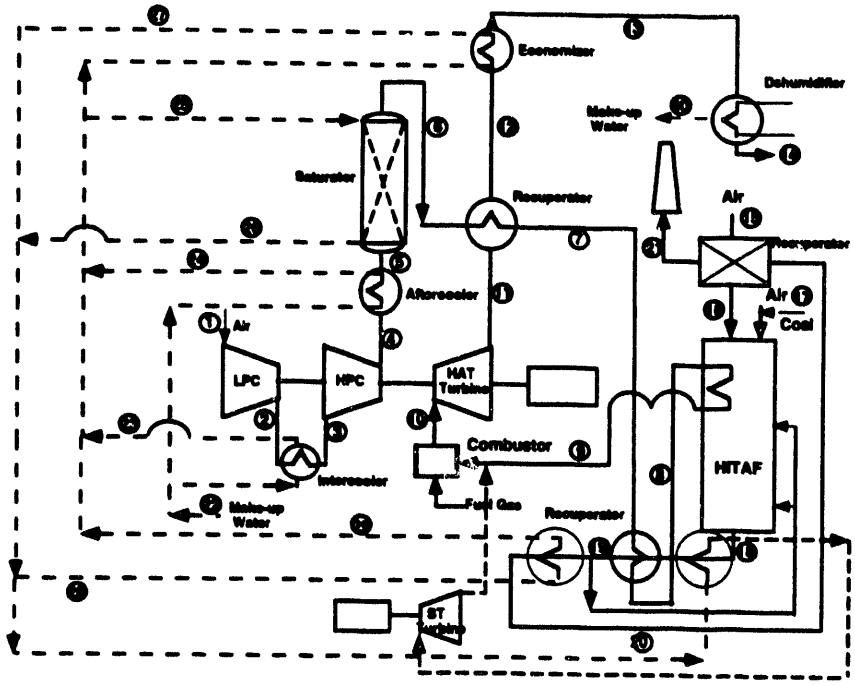

Figure 2. Coal–Fired HITAF HAT Cycle with Steam Topping.

CHEMICAL REACTOR MODELING

The 100,000 Btu/hr test facility at the University of Utah is being used to evaluate combustor design concepts related to the HITAF long-flame design. Firing system concepts (such as burner design and the impact of vitiated air) and NO_x control strategies (such as staging, reburning and SNCR) can be evaluated independently or in concert with the "U"-shaped furnace (see Quarterly #4 for the period January-March 1993 for a detailed description of the "U"-shaped furnace). Many experimental configurations have been evaluated to date and brief description of some of these will be given here.

Process Simulation

As one of the goals of the "U" furnace is to simulate HITAF conditions, it is important that the facility be capable of achieving the high temperatures associated with the current design of the HITAF. In particular, gas temperatures in excess of 2800°F in the radiant zone and temperatures near 1800°F in the SNCR zone. A plot of temperature measurements obtained in the "U" furnace at two different firing rates is shown in Figure 3. As shown, both conditions have been achieved and some control over the temperature in the SNCR zone can be attained with variations in the firing rate. Additional control may be achieved with the use of cooling coils.

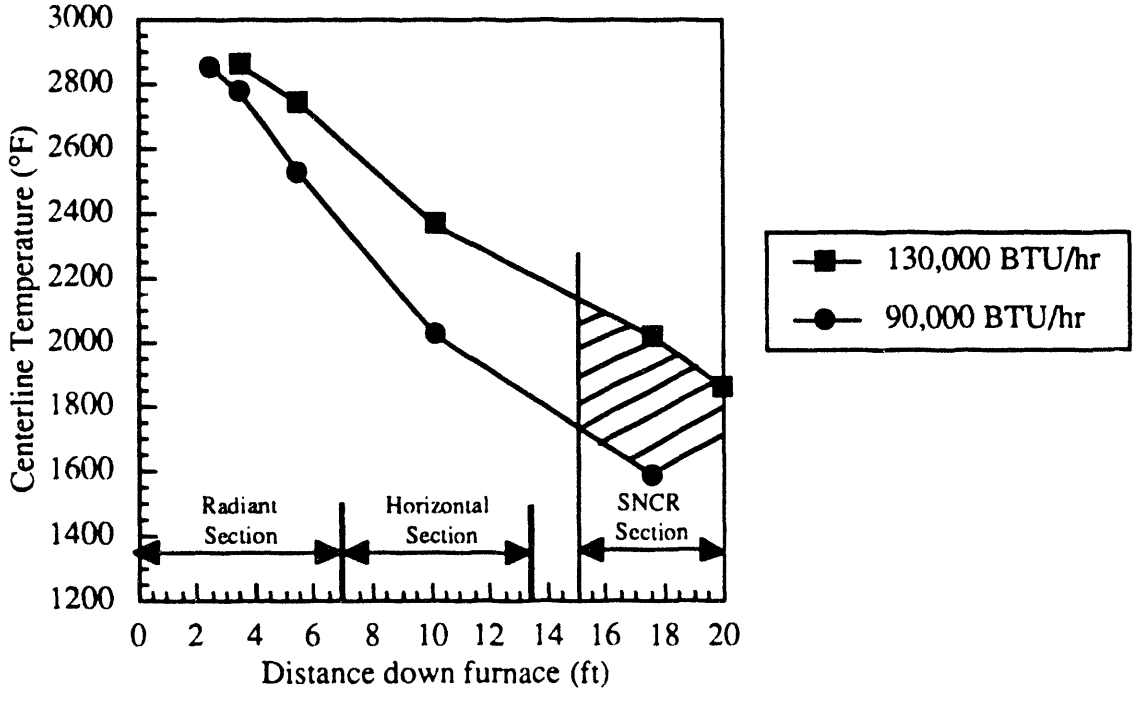

Figure 3. Centerline gas temperature measured in the "U" furnace at two different firing rates.

Staging/Reburning

The ability of primary zone air staging to control NO_x emissions with the long axial flame has been investigated with parametric variations in both the primary zone stoichiometry and residence time prior to burnout air addition. The results of the studies are shown in Figure 4. Data is presented for two different primary zone residence times including two data sets for the shorter residence time. Six different primary zone stoichiometries were evaluated. The furnace was fired at a rate of 130,000 Btu/hr with stabilization gas comprising 9% of the total fuel input, and primary air at 10% of total air input (not vitiated) with an overall stoichiometry of 1.15. An analysis of the results indicates the need to optimize residence time in the staged zone with respect to primary zone stoichiometry. At very high or very low stoichiometries, the effect of residence time on NO emissions is minimal. At stoichiometries near the design point for the HITAF, however, the effect of residence time is much more pronounced. At a stoichiometry of 0.85, there is a 50% increase in NO_x emissions with a 30% decrease in residence time.

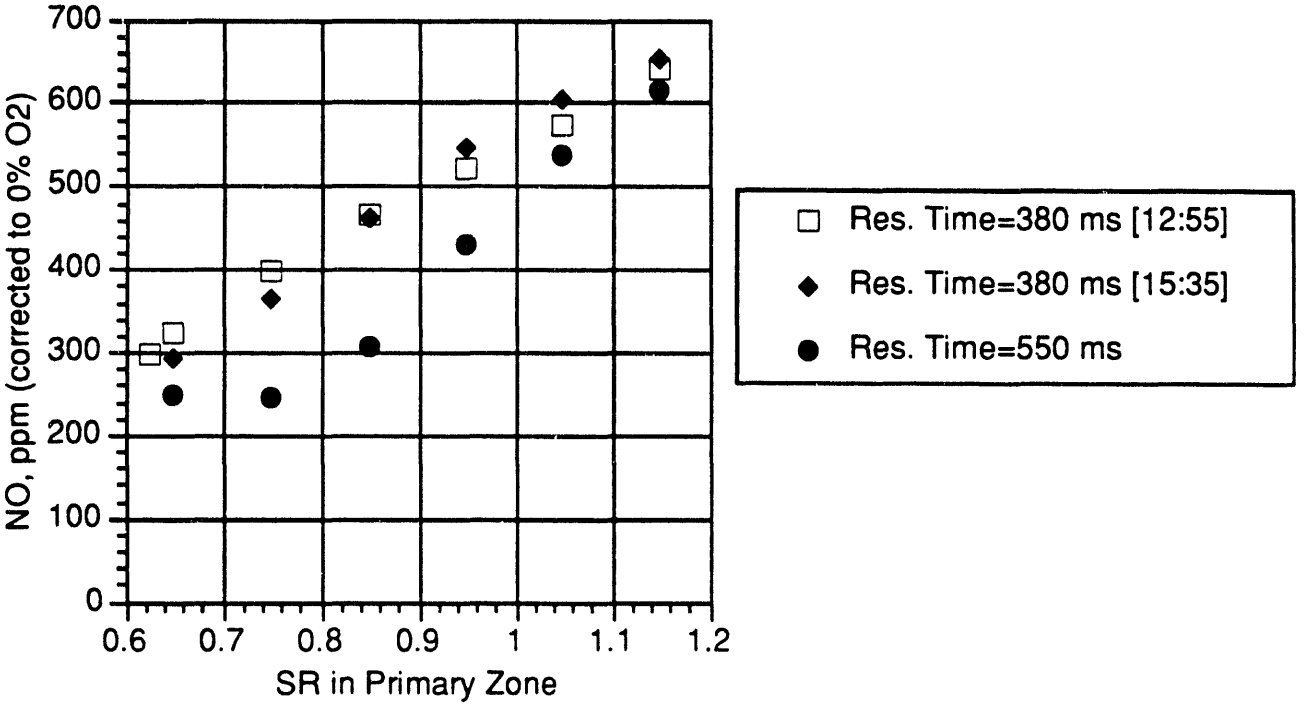

Figure 4. The effect of primary zone residence time on NO emissions in the "U" furnace. Firing rate was 130,000 Btu/hr with an overall stoichiometry of 1.15.

Figure 5 shows staging results under different furnace operating conditions. The firing rate was decreased to 121,000 Btu/hr with the stabilization gas reduced to 5% of the total fuel input; however, the primary air was increased to 15% of the total air input. As shown in Figure 5, the NO emissions can still be optimized with respect to primary zone stoichiometry; however, the overall NO emission levels are higher than for the furnace conditions in Figure 4 (lower primary air percent and higher percent stabilization gas).

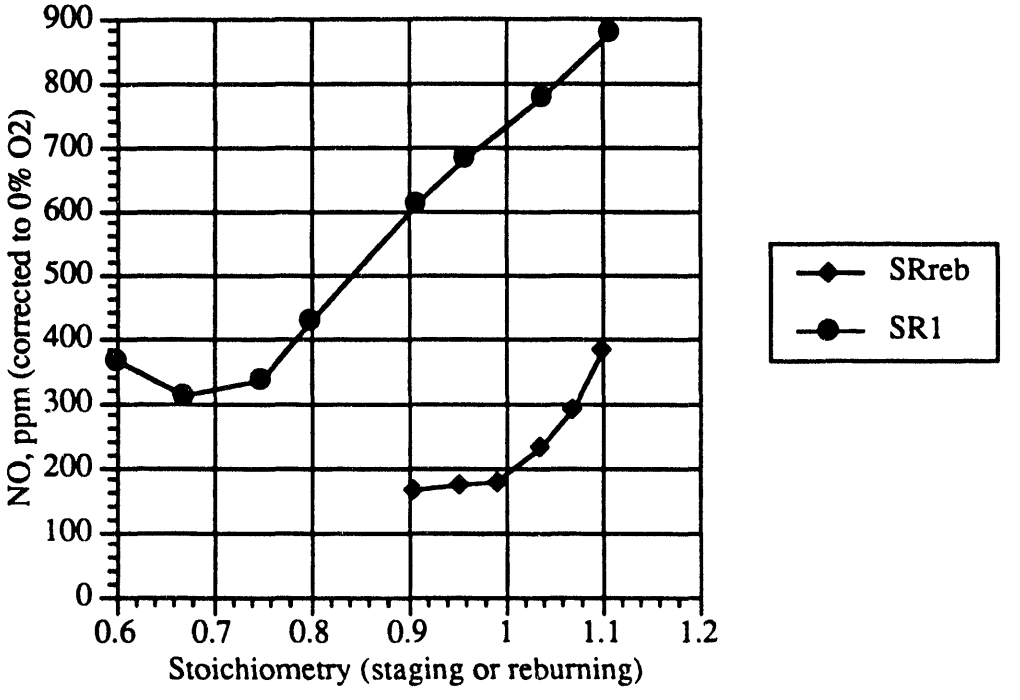

Figure 5. Comparison of NO reduction by staging and staging/reburning. Firing rate was 121,000 Btu/hr.

Figure 5 also shows the impact of reburning on NO emissions. In addition to demonstrating the ability to achieve less than 200 ppm NO from a pulverized coal flame, the reburning data also illustrate a limitation on the amount of gas addition that would be useful for reburning. As additional natural gas is introduced to lower the reburning stoichiometry much below 1.0 (when starting at 1.1), the effectiveness is minimal; therefore, there may be a limit on the amount of natural gas addition needed for effective reburning. The limited gas addition is particularly relevant to the HITAF as the current design and cycle analysis allows little, if any, natural gas to be used for reburning.

Vitiated Air

The "U" furnace has been designed for flexibility to allow independent variation of various parameters. The combustion air temperature and extent of vitiation can be varied by the combined use of electric preheaters and a natural-gas-fired preheater. Additional control of O_2 concentration, independent of temperature, is obtained by direct oxygen injection into the vitiated air stream prior to entering the primary coal burner. The effect of varying oxygen concentration at approximately a constant combustion air temperature was evaluated and the results are shown in Figure 6. The furnace was operated under mildly staged conditions (primary zone stoichiometry was 1.05) with an overall stoichiometry of 1.15. As shown, there is an increase in NO emissions with increasing oxygen content in the combustion air. The use of vitiated air, therefore, leads to lower NO emissions at a given stoichiometry.

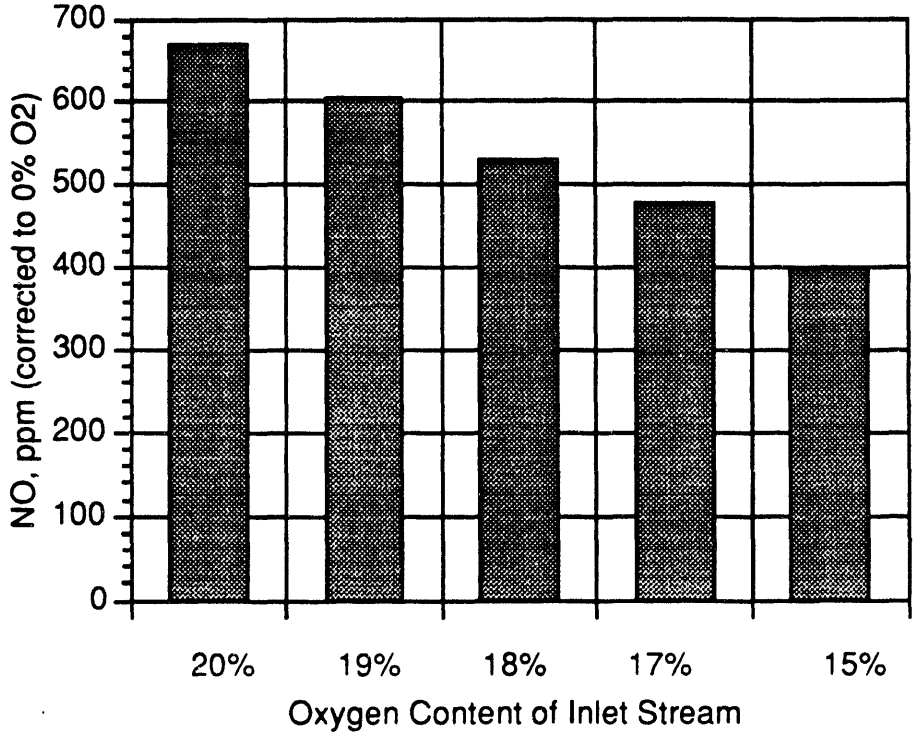

Figure 6. Impact of the degree of vitiation on NO emissions in the "U" furnace. Primary zone stoichiometry was 1.05, overall stoichiometry was 1.15.

In general practice, however, it is not a simple matter to control both temperature and oxygen independently as direct oxygen injection is an expensive addition to a large, coal-fired facility. Although decreasing the oxygen concentration lowers NO_x emissions, the decreased O_2 also lowers the flame temperature. The decrease in thermal input due to the use of vitiated air must be offset, therefore, with an increase in enthalpy via a higher preheat for the oxygen-depleted air. The thermal

trade-offs between the use of 'normal' combustion air (21% O_2 at 600°F) and the proposed combustion air (17.6% O_2 at 1010°F) need to be considered. Equilibrium calculations of adiabatic combustion of a bituminous coal in the two different air streams, shown in Figure 7, indicate that the high-temperature vitiated combustion air anticipated for use with the HITAF yields approximately the same flame temperature as the standard preheat of non-vitiated air.

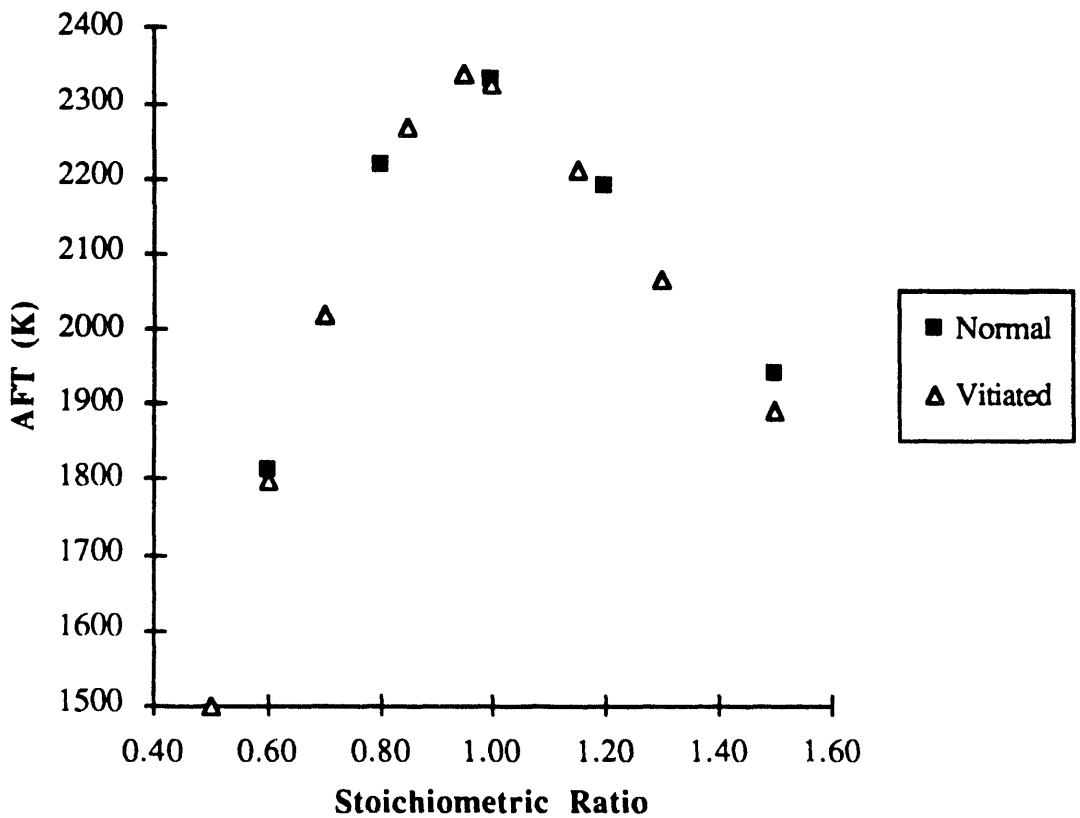

Figure 7. Adiabatic flame temperatures for a bituminous coal burned with "normal" combustion air (21% O_2 – 600°F preheat) and "vitiated" combustion air (17.6% O_2 – 1010°F preheat).

As these two air streams yield similar performance on a thermal basis, it is of interest to determine the benefits that may arise from using the oxygen-depleted combustion air, albeit at a higher temperature. Figure 8 presents data obtained from two different test series where the impact on NO emissions from using "normal" air versus "vitiated" air was evaluated under staged conditions. The furnace was operated at a firing rate of 90,000 Btu/hr using 9% of the fuel input as stabilization gas. 15% of the total air input was introduced in the primary stream and the overall stoichiometry was 1.15. As shown in Figure 8, the decrease in NO emissions with decreasing primary zone stoichiometry is less pronounced for the vitiated air case, as might be expected. Since the vitiated combustion air has

a much lower oxygen content, it is reasonable that the vitiated case would exhibit a lesser sensitivity to staging, or in other words reducing the oxygen content, in the primary zone.

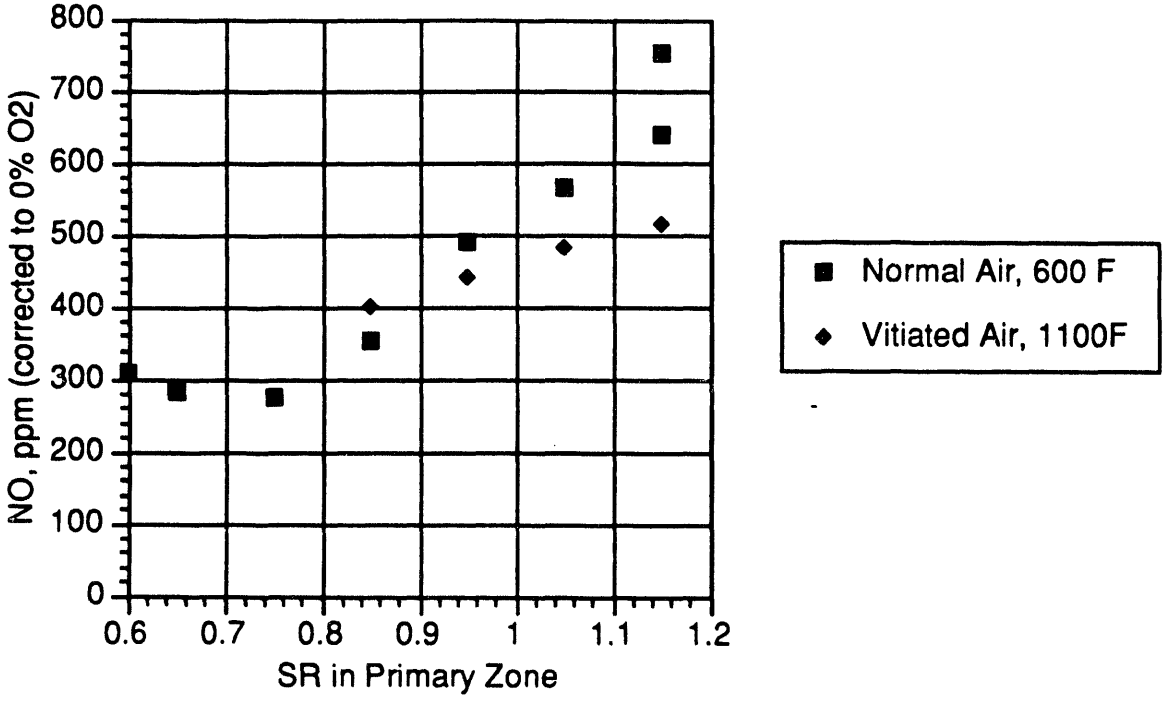

Figure 8. Comparison of high-temperature vitiated combustion air and standard combustion air under staged conditions.

In addition, the experimental results indicate that at stoichiometries near design for the HITAF, the difference in NO emissions resulting from the two types of combustion air is minimal. This effect was also verified by use of the comprehensive coal combustion model where the comparison between the two types of combustion air was compared at a stoichiometry near 1.0. The model was used to predict the observed effect in the full-scale HITAF. The results from the model predictions, shown in Figure 9, indicate a trend similar to the experimental observation whereby the difference between the two cases is minimal. The NO emissions from the model are also lower overall; however, the model predictions did not include the burnout air addition to bring the stoichiometry up to 1.15.

NO Formation in Coal Flames

The processes occurring during the combustion of pulverized coal particles that affect the fate of coal nitrogen are illustrated pictorially in Figure 10. For simplicity, a pulverized coal flame has been divided into three regions: 1) preignition; 2) volatile heat release, and 3) char burnout. The preignition region covers the time the coal particles leave the injector until there is significant volatile ignition. In this region the coal particles are heated primarily by convection as they mix with the secondary air. The

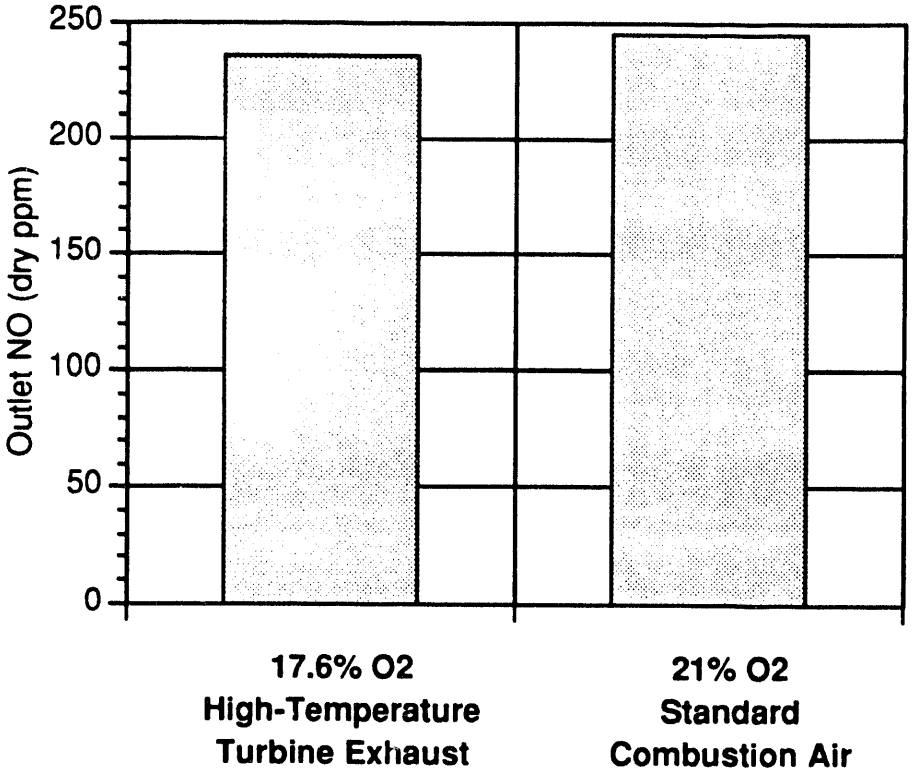

Figure 9. Model predictions comparing high-temperature vitiated combustion air (1010°F) and standard combustion air (650°F).

secondary air also mixes with high temperature furnace gases. As the particle temperature rises, volatile combustible gases are released. When the volatiles reach a critical concentration and temperature, they ignite in the volatile heat release region consuming all the oxygen. Further increases in particle temperature result in the release of more volatiles which burn when they contact oxygen, as the coal jet mixes with the vitiated secondary air flow. In the third region, all of the volatiles have been consumed and the char burns out. This figure is an obvious simplification; it neglects the complexity of turbulent transport, two phase flow and the temporal variations that occur in turbulent diffusion flames. However, it serves to illustrate how both coal quality and operational parameters effect NO emissions.

The volatile nitrogen compounds are rapidly converted to HCN and their ultimate fate is dependent on the availability of oxygen. In the presence of oxygen they form NO; but in the absence of oxygen the formation of molecular nitrogen is favored. Under rich conditions the volatile fuel nitrogen compounds are converted to N_2, NO, NH_3 and HCN. The nitrogen speciation and the fraction converted to NO is dependent on temperature, gas phase stoichiometry and coal type. It is believed that homogeneous and heterogeneous NO reductions occur within the pores of the char particle and this is one reason that char nitrogen conversion to NO is less than the conversion of the volatile fuel nitrogen fraction.

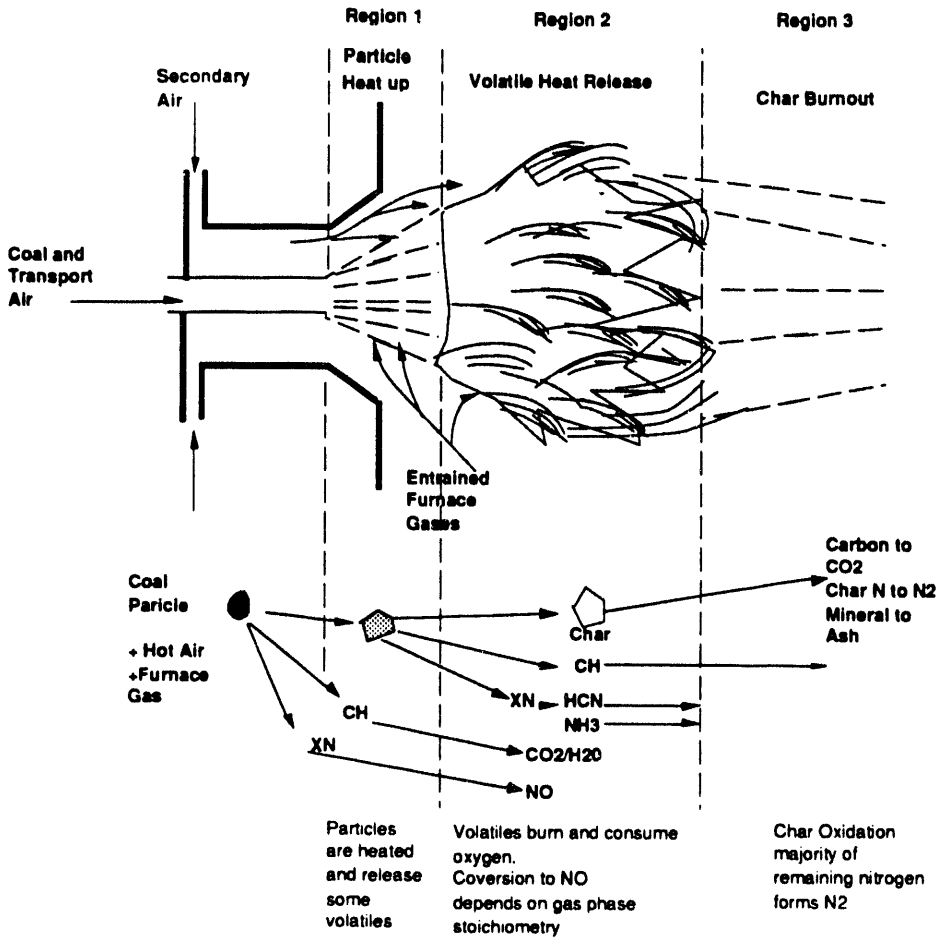

Figure 10. Pathways for NO formation in a pulverized coal flame.

Based upon this simplistic overview it might be expected that, under excess air conditions, the following coal parameters will increase NO formation:

- Higher volatile fuel nitrogen release; either because of higher initial nitrogen content or because higher temperatures promote volatile evolution.
- Increased char nitrogen content.
- Volatile combustible release; because this decreases the availability of oxygen in the volatile heat release region.

Under staged conditions, retention of char nitrogen will reduce the effectiveness of staging. If char nitrogen conversion takes place, it must occur during burnout. The formation of molecular nitrogen from the volatile fuel nitrogen species depends upon gas phase stoichiometry and temperature. Since there is a difference between volatile and char nitrogen conversion efficiency, NO

formation from fuel nitrogen conversion should be affected by those operational parameters that control the partitioning of coal nitrogen into the volatile and char fractions. In addition, since volatile nitrogen conversion is dependent on oxygen availability, fuel NO formation would be expected to be highest when the coal particles are hottest and well mixed in an atmosphere containing excess oxygen.

Figure 11, taken from the work of Pershing et al. (1990), shows the influence of oxygen availability on the conversion of both volatile and char nitrogen to NO. Oxygen availability was controlled by using three different burners. The oxygen availability is maximum under premixed conditions and minimum in the axial diffusion case because of the delay in coal/air mixing. Fuel nitrogen conversion in the coal decreases with a decrease in oxygen availability; that is, premixed>radial diffusion>axial diffusion. The conversion of char nitrogen is unaffected by the initial burner conditions presumably because, regardless of the initial conditions, char oxidation takes place in a very similar environment. However, the conversion of the volatile nitrogen fraction, determined from mixtures with and without ammonia, decreases dramatically as oxygen availability is reduced.

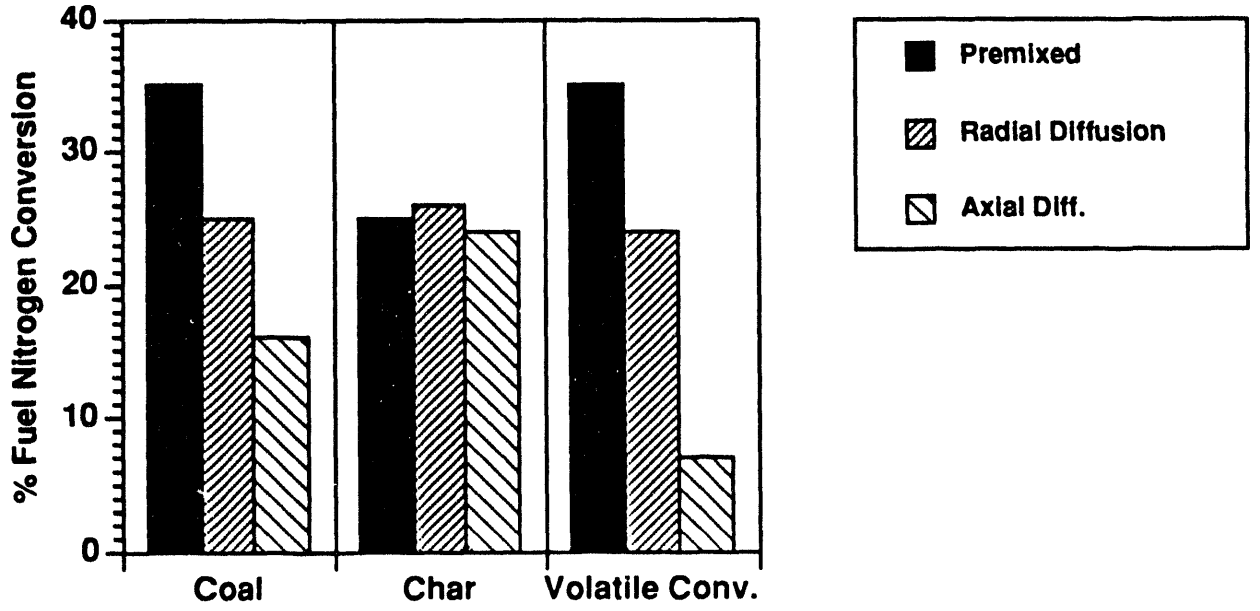

Figure 11. The influence of mixing conditions on fuel nitrogen conversion.

Operational parameters that affect the availability of oxygen in the flame will have a major impact on the emission of NO. Increasing oxygen availability will increase NO emissions. Parameters that affect the thermal environment are more confusing. Increasing temperature should increase NO

emissions but the effect may also be dependent on the availability of oxygen and it may be difficult to separate the effects of temperature and mixing.

Ignition Effects

Returning to Figure 10, it is now possible to explain the importance of the preignition region because this has a major impact on oxygen availability in the volatile heat release region. If the primary air to coal ratio is constant, then the location of the ignition zone will dictate the amount of oxygen from the secondary air stream that mixes with the coal jet. If the ignition front is located at or very close to the fuel injector, most of the oxygen will be consumed by the volatile diffusion flame that surrounds the coal jet and therefore will not be available to mix with subsequent devolatilizing coal particles. Location of the ignition zone is dependent on many factors, including:

Burner design: the amount of swirl, the relative velocity of the primary and secondary jets. Heap and Folsom (1990) report a decrease in NO emissions of 130 ppm from an initial value of 400 ppm when the ignition distance was changed from zero to thirty centimeters by increasing the velocity of the secondary air stream for the same coal burning in the same furnace under the same conditions.

Coal particle size: an increase in the amount of small particles will promote early ignition.

Temperature: increasing the preheat temperature will promote early ignition because of the impact on volatile release.

Coal volatile content: all other conditions being equal, the ignition distance will increase with decreasing volatile content. Thus a low volatile coal might have a lower nitrogen content than a high volatile coal but the NO emissions are higher because the increased ignition distance increases the availability of oxygen in the volatile release region.

Furnace conditions affect the flame temperature because they affect both the radiative loss from the flame and the temperature of the bulk gases entrained by the secondary air stream.

Modeling the Ignition Front

It is apparent from the previous discussion that an accurate prediction of NO formation in pulverized coal flames requires the ability to accurately predict the preignition distance of stand-off distance for a given set of operating conditions. As the current HITAF design consists of a long axial flame, the ability of predicting the ignition front of such a flame becomes a critical issue.

A large, pilot-scale HITAF has not yet been constructed that would provide necessary data on ignition behavior for long flames; subsequently, a data source was sought in the literature that would

describe the ignition phenomena of long axial coal flames at a reasonably large scale. The dataset of Michels and Payne (1988) taken on the International Flame Research Foundation (IFRF) is a fairly comprehensive dataset and was taken at a firing rate of 7 million Btu/hr. The data consists of both unattached and attached flames; therefore, a considerable range of ignition phenomena could be investigated.

The ability of the comprehensive coal combustion codes to predict the ignition fronts of two of the test flames, A1 (attached) and B1 (unattached), was evaluated using the axisymmetrical combustion code, *JASPER*. The measurement utilized to evaluate the performance of the code was the centerline gas temperature measurement. The results for Flames A1 and B1, shown in Figures 12 and 13 respectively, illustrate the ability of the code to accurately predict the location of the initial temperature increase and subsequently the flame front.

The overall agreement between data and model is very good with the exception of the peak temperatures. It should be noted here, however, that the figures shown may not reflect a true comparison per se. The model results present the true gas temperature as computed by the code – wholly separate from the temperature of the burning particles. It is much more difficult, however, to

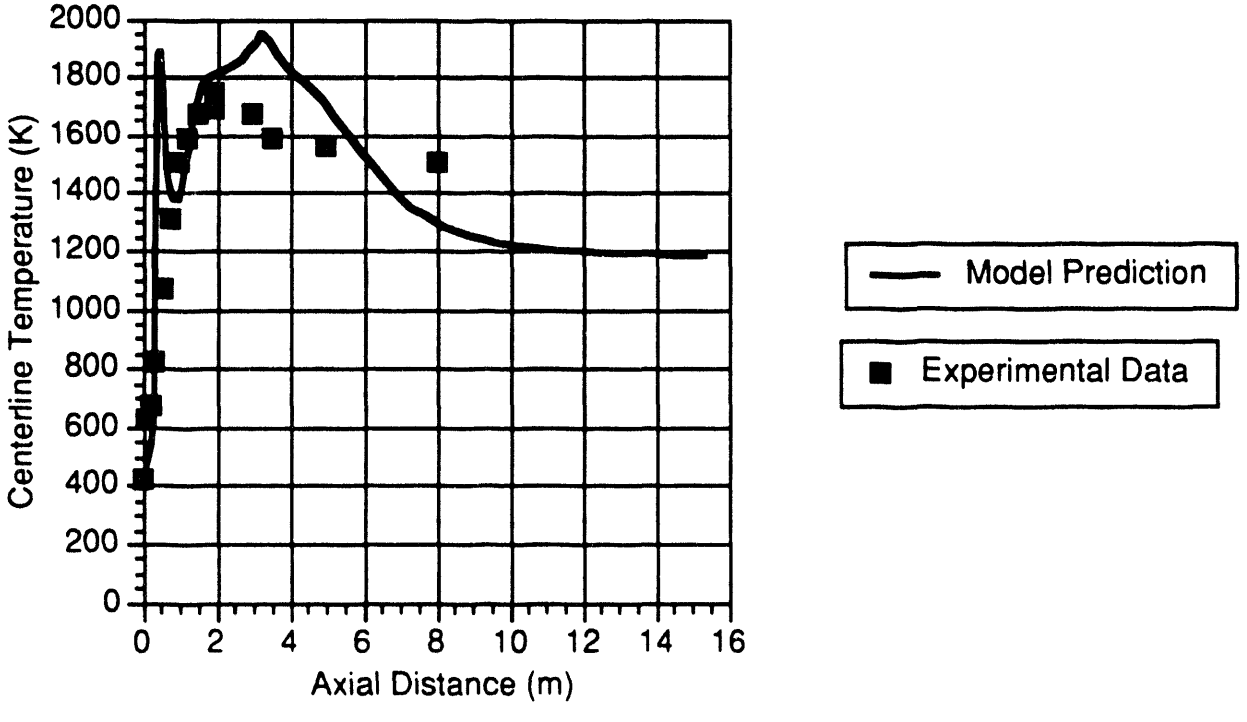

Figure 12. Comparison of measured and predicted centerline temperatures for the attached long axial flame (A1) in the 7 million Btu/hr IFRF furnace.

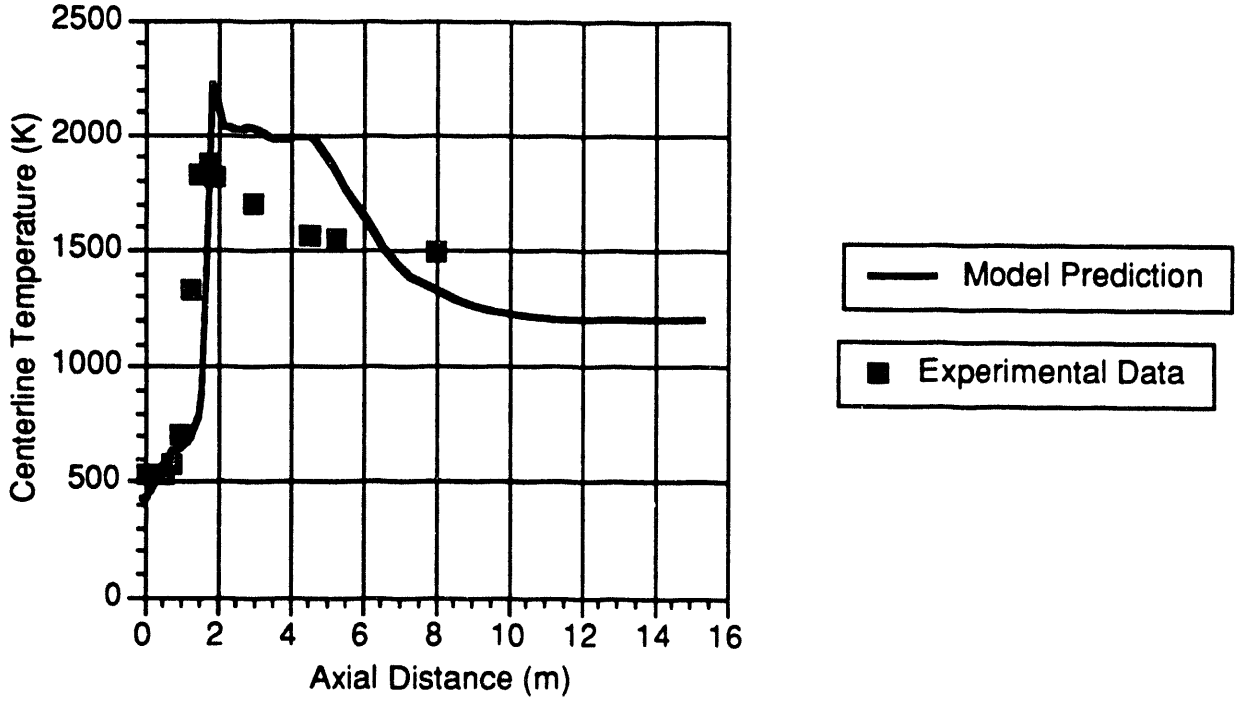

Figure 13. Comparison of measured and predicted centerline temperatures for the unattached long axial flame (B1) in the 7 million Btu/hr IFRF furnace.

measure a true gas temperature in a coal flame. The data points actually represent a combination of gas and coal particle temperatures.

To assist in understanding the differences, the separate gas and particle temperatures for the five different particle sizes used in the *JASPER* computation are shown in Figure 14. The particle size (in microns) and the weight percent corresponding to that size are printed on each figure. Also, the upper or higher temperature curve in each figure is the gas temperature surrounding the given particle trajectory down the length of the furnace, and the lower temperature curve (where distinguishable) corresponds to the particle temperature. For the small particles, the two temperatures are similar; however, for the large particles, which have significant thermal mass, the two temperatures are notably different. As the temperature measurement (suction pyrometer probe) draws in both gas and particles, the temperature reported necessarily reflects some combination of the two.

Perhaps more importantly, however, is the necessity of a predictive model to be able to make the distinction between the two temperatures. To accurately predict the preignition distance, the true particle temperature (including effects of radiation) must be accurately predicted to obtain the proper extent of devolatilization for each particle size and subsequently the onset of ignition. The amount of combustion air thus entrained into the primary jet prior to ignition can then be predicted and the correct environment for fuel nitrogen oxidation can be computed.

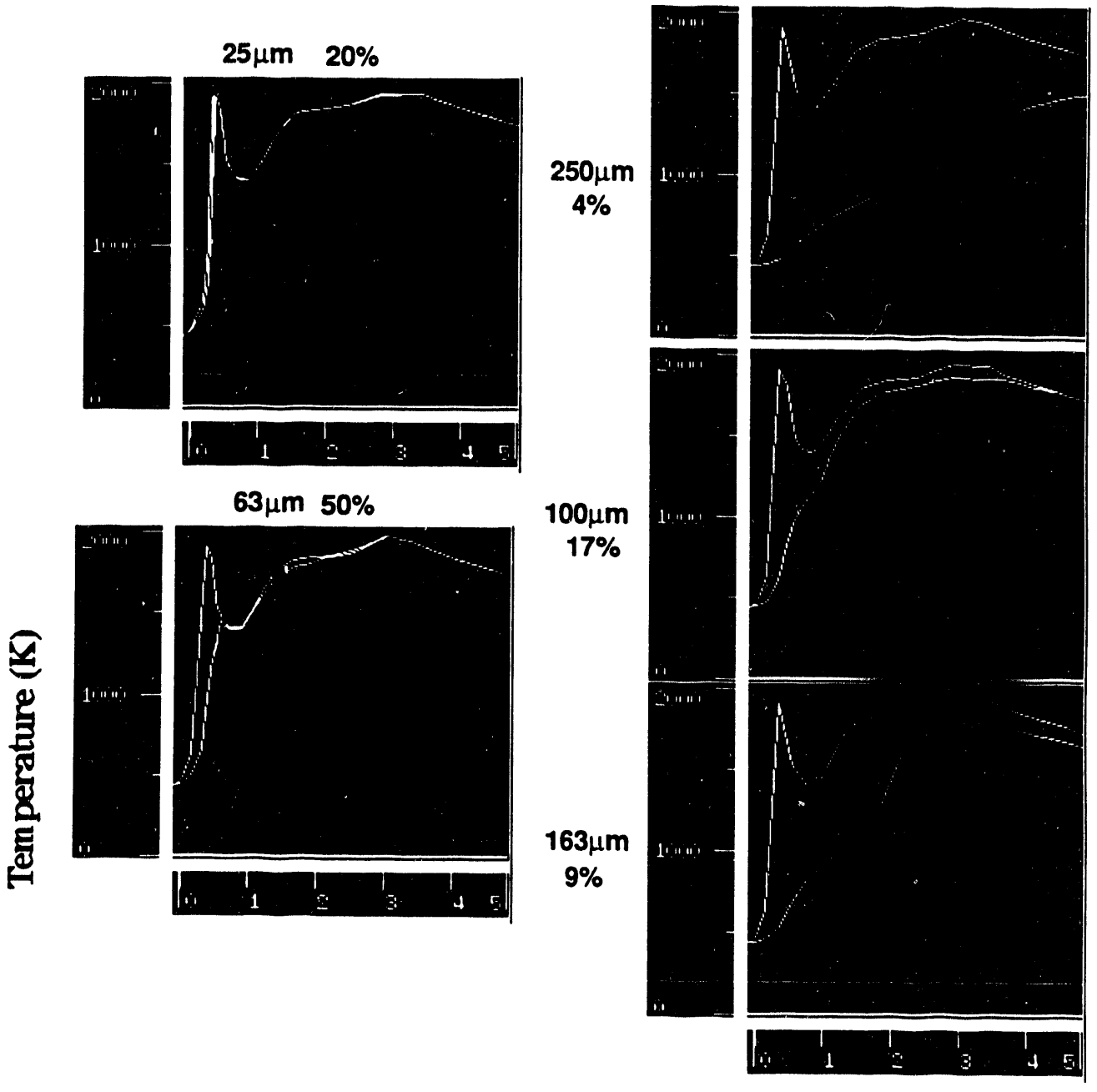

Figure 14. Gas and particle temperatures along the centerline (in meters) of the 7 million Btu/hr long axial flame of the IFRF furnace tests. Different particle sizes are shown with the corresponding weight percent representing that particle size. The lower temperature (where distinguishable) corresponds to the particle temperature.

ASH DEPOSITION RATE CALCULATIONS FOR HITAF CONVECTIVE AIR HEATER

Computational fluid dynamics (CFD) has been used to analyze the particle–laden flow within the HITAF convective air heater to provide estimates of the rate of deposition of particulates on the heat exchanger surfaces. Results for particle trajectory calculations conducted for various convective air heater configurations have been described previously (April –June, 1993 Quarterly). The finned–tube–sheet design chosen for this study is shown in Figure 15. The tube sheets are spaced 4 in. apart and consist of 1 in. I.D. cylindrical tubes spaced 3 on center in the baseline design. Four variants of this design have been evaluated with the objective of minimizing ash deposition on the surfaces of the heat exchanger. The four designs are:

1) In–line cylindrical tubes (Fig. 16)

2) Staggered cylindrical tubes (Fig. 17)

3) In–line, 5:1 aspect ratio ellipsoidal tubes (Fig. 18)

4) Staggered, 5:1 aspect ratio ellipsoidal tubes (Fig. 19)

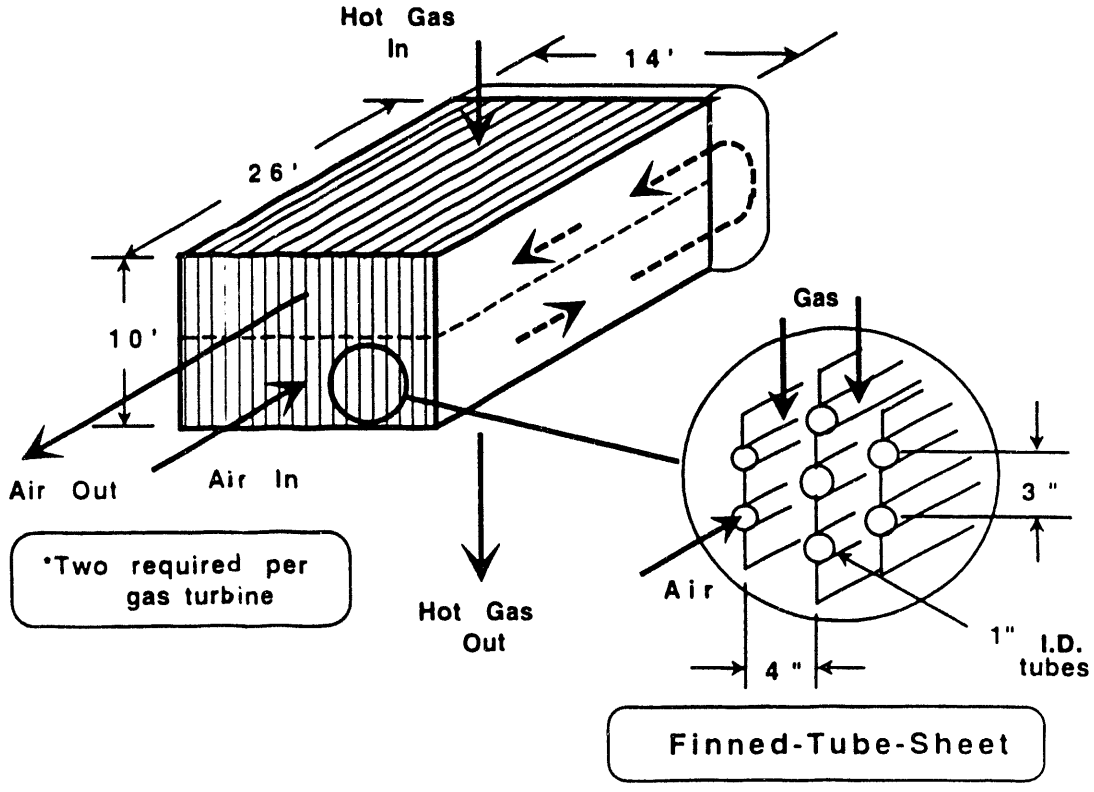

Figure 15. Convective air heater. Configuration/dimension.

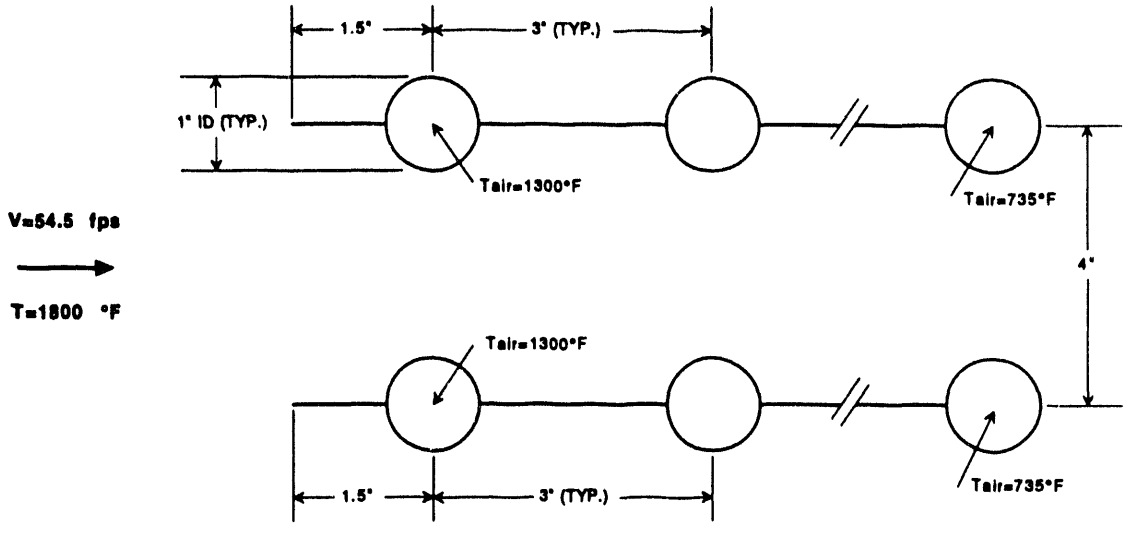

NOTES: 1) Repeat pattern 40x for a total length of 10 feet
2) Tube thickness 0.25"
3) Fin (or web) thickness 0.50"

Figure 16. Convective air heater, in-line tube array.

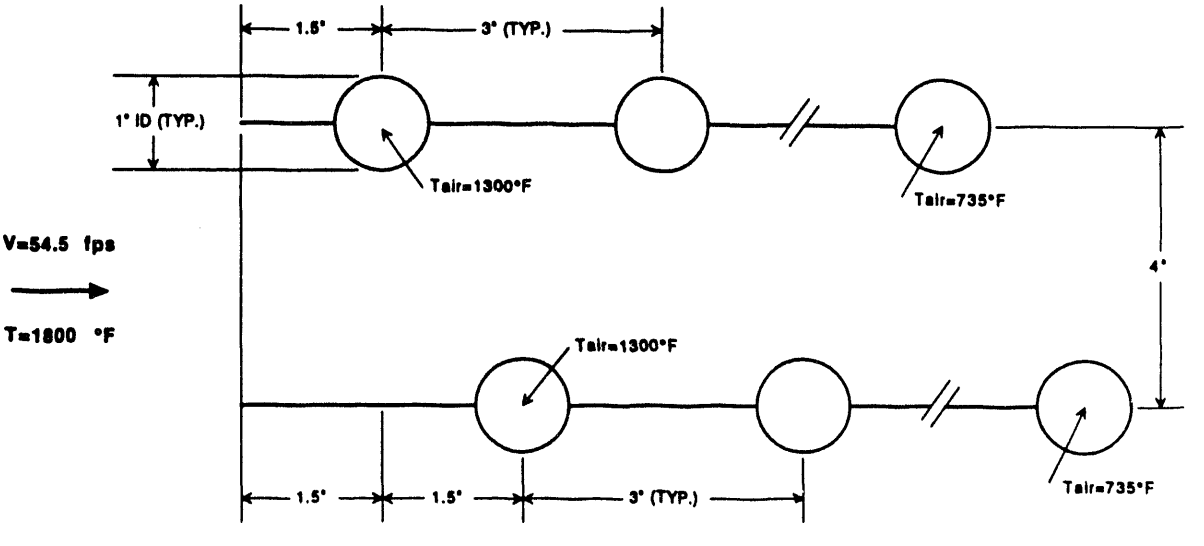

NOTES: 1) Repeat pattern 40x for a total length of 10 feet
2) Tube thickness 0.25"
3) Fin (or web) thickness 0.50"

Figure 17. Convective air heater, staggered tube array.

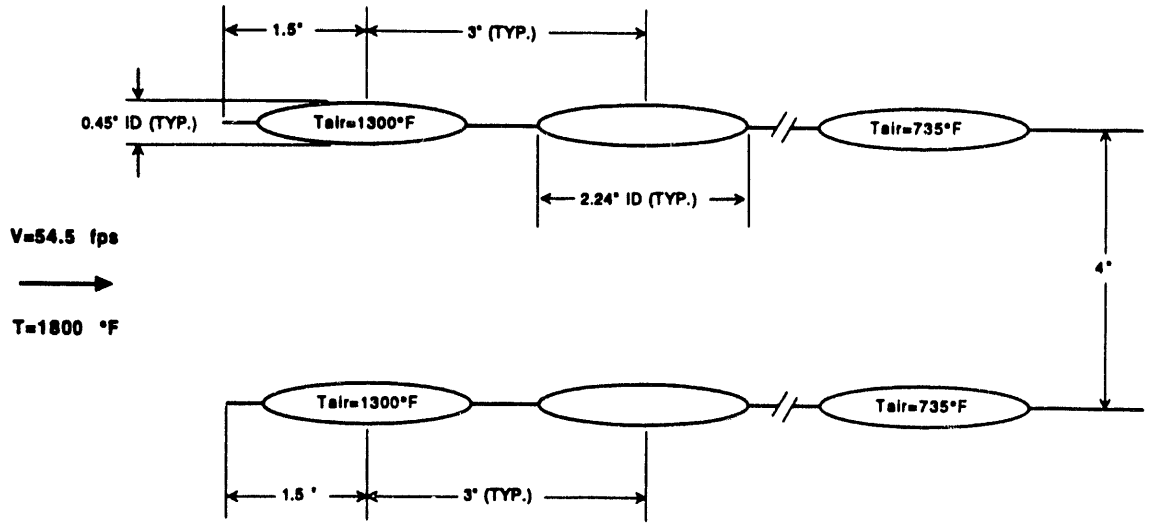

NOTES: 1) Repeat pattern 40x for a total length of 10 feet
2) Tube thickness 0.25"
3) Fin (or web) thickness 0.50"

Figure 18. In-line tube array – 5:1 aspect ratio ellipsoidal tubes.

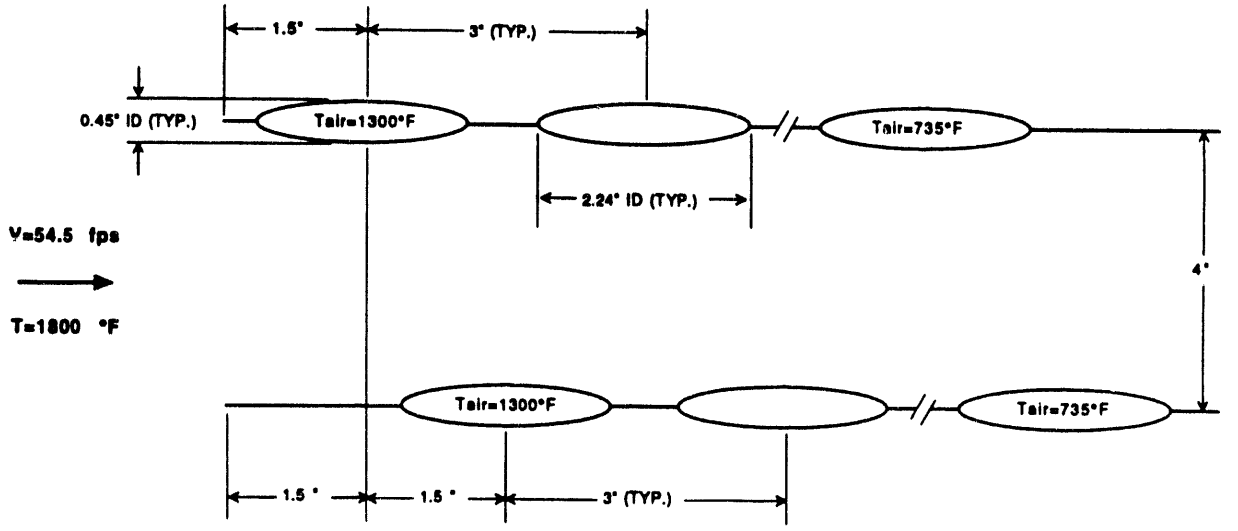

NOTES: 1) Repeat pattern 40x for a total length of 10 feet
2) Tube thickness 0.25"
3) Fin (or web) thickness 0.50"

Figure 19. Staggered tube array – 5:1 aspect ratio ellipsoidal tubes. tubes.

Note that the elliptical tubes have been sized to provide the same cross-sectional area as the cylindrical tubes. The hot gas inlet conditions are: p = 1 atm, T = 1800°F and V = 54.5 ft/s. Air temperatures inside the tubes are 1300°F and 735°F at the hot gas inlet and outlet of the heat exchanger, respectively. Wall temperatures are estimated to be 1445°F and 885°F at the inlet and outlet, respectively. Two cases for ash particle mass loading are given in Table 2.

Table 2. Ash Particle Size Distribution at Inlet of HITAF Convective Air Heater

PARTICLE SIZE RANGE (μm)	Ash Loading [kg/m^3] Case 1 (before Slag Screen)	Ash Loading [kg/m^3] Case 2 (after Slag Screen)
1 – 2.5	7.71E-06	9.31E-06
2.5 – 5	8.96E-05	1.08E-04
5 – 10	2.40E-04	2.60E-04
10 – 20	3.69E-04	1.78E-04
20 – 40	3.08E-04	0
40 – 80	1.38E-04	0
TOTAL	1.15E-03	5.55E-04

The geometry and flow conditions analyzed for the ash deposition rate calculations are listed in Table 3. All cases were run with an inlet velocity of 54.5 ft/s and an inlet temperature of 1800°F.

Table 3. Geometry And Flow Conditions

Case	Cross section	Number	Arrangement	Turb. Int. percent	T_w °F
HX3	Circ.	3	Inline	10	1445
HX4	Circ.	3	Staggered	10	1445
HX6	Ellip.	3	Inline	10	1445
HX7	Ellip.	3	Staggered	10	1445

Particulate deposition rates were obtained by assigning a spatially uniform distribution of particles at the inlet plane; the particle size distribution was representative of distributions with or without slag screens. Particle trajectories were calculated stochastically using hundreds of computational particles for each size class.

Ash deposition rates for cases HX3, and HX6 are presented in Figs. 20-21, respectively. Results are presented for six particle sizes: 1.25, 3.75, 7.5, 15, 30 and 60 μm. Each pair of bars on the Figures represents the average mass deposition rate on a one inch long (in the flow direction) axial segment

(a)

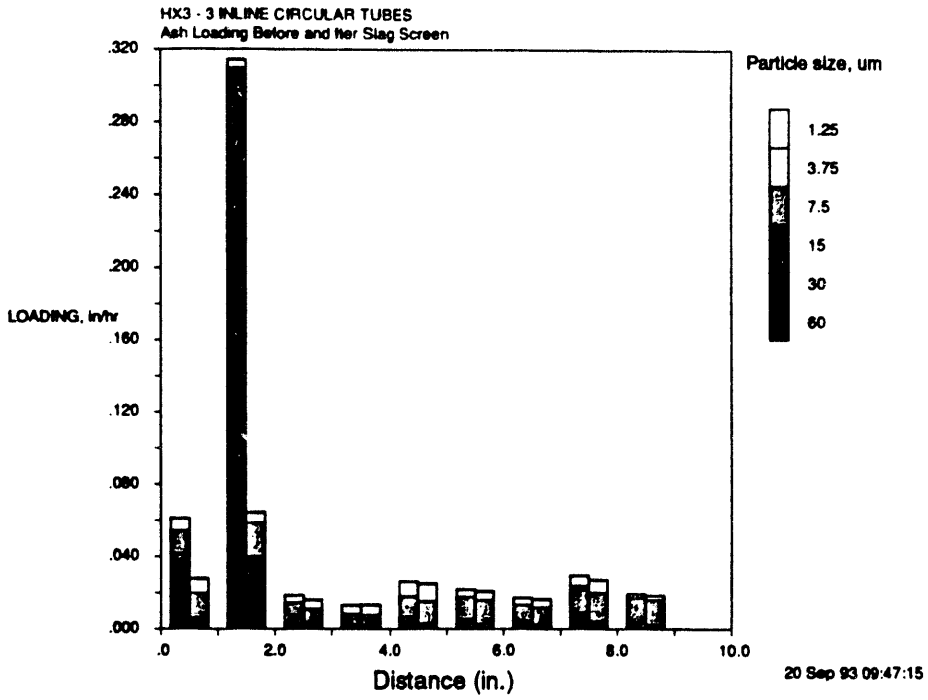

(b)

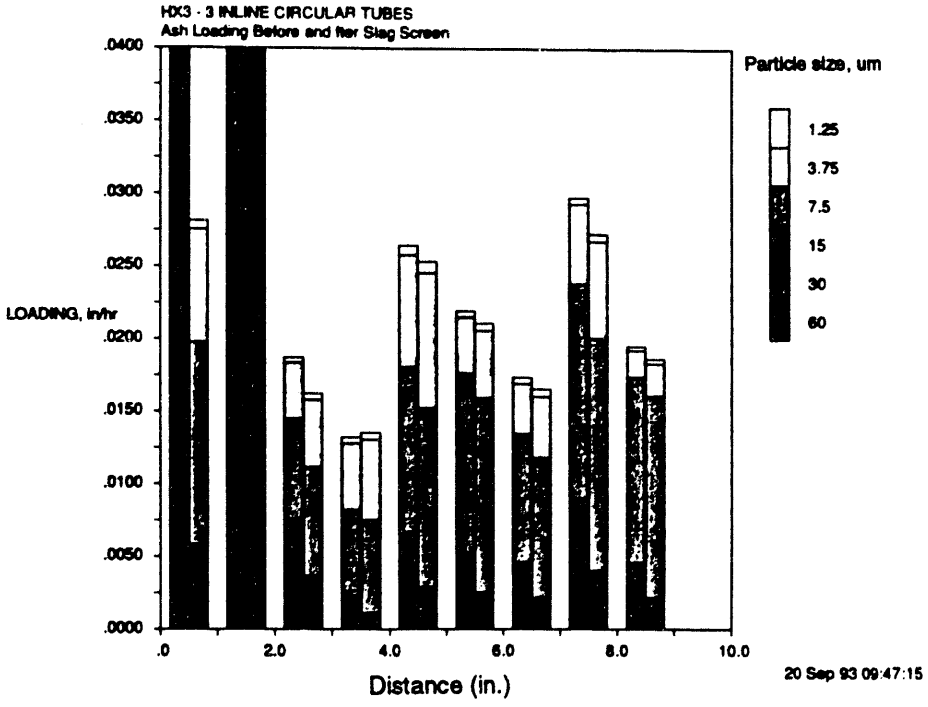

Figure 20. HX3-3 inline circular tubes.

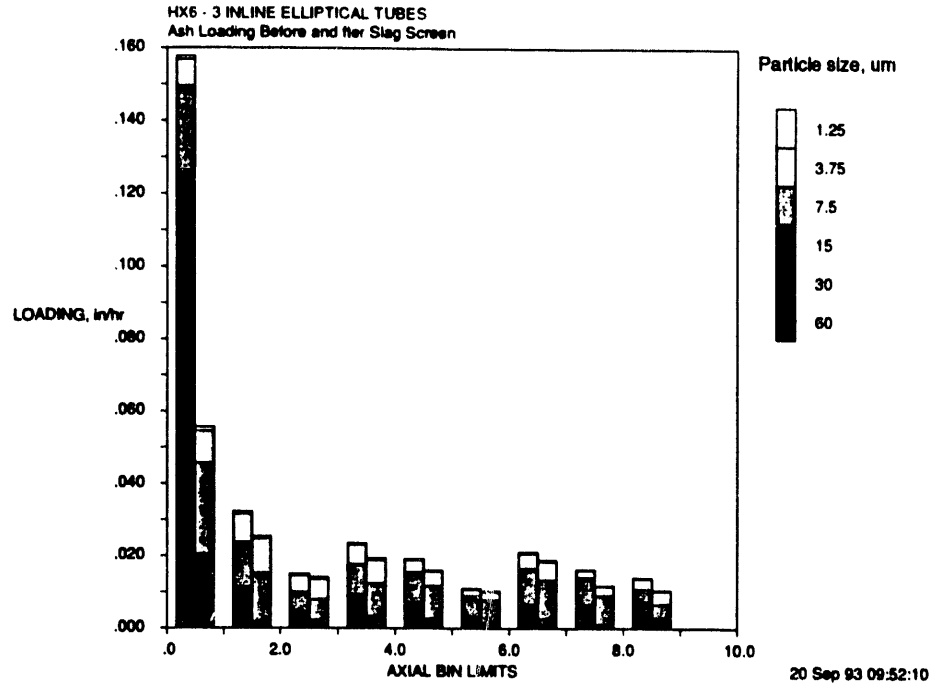

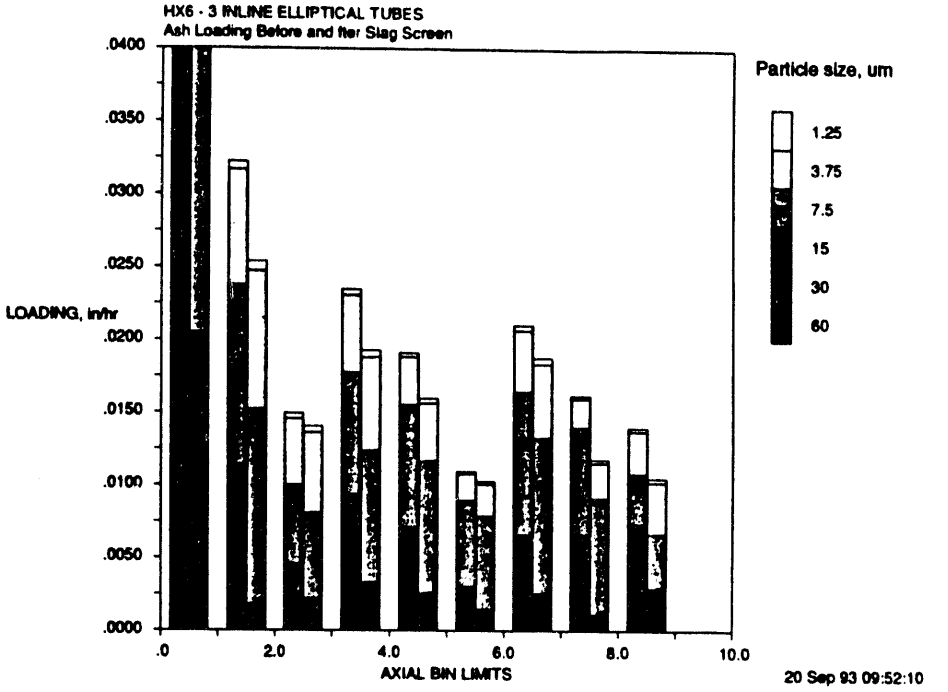

Figure 21. HX6-3 inline circular tubes.

(axial bin) of the heat exchanger surface. The left–most bar in each pair displays the results for the ash loading without a slag screen, while the right–most is for that with a slag screen. Note that the vertical axis of part a of the Figures is scaled to show the maximum deposition rate, which always occurs at the upstream face of the first tube in the array. Part b of the figures is simply an expanded view which allows the smaller deposition rates on downstream tubes to be discerned.

The results show that the highest deposition rates occur on the first tube and that this rate is about a factor of two higher for the circular tubes than for the elliptical ones. There is no significant difference in deposition rates between the in–line and staggered configurations. Of course, the present analysis does not account for the reduction in cross–sectional flow area which will occur as the deposits build on the tubes. Conceptually, the staggered arrangement should be advantageous in this regard. The first tube captures the majority of the 15 μm and larger particles in the flow. The presence of a slag screen upstream of the heat exchanger serves to eliminate particles greater than about 20 μm which results in a factor of two reduction in the particulate mass loading of the heat exchanger inlet stream. The resulting reduction in the deposition rate on the first tube is a factor of four for circular tubes and a factor of three for elliptical tubes. These results clearly show that a slag screen should be included in the design and also that it will be beneficial to replace the first tube with a sacrificial circular rod that can be used to remove the larger particles that are otherwise likely to impinge on the heat exchanger.

Deposition rates on the downstream tubes, about 0.025 inches/hr, are over an order of magnitude lower than for the first tube. The analysis is conservative, since 100% sticking is assumed (impaction=deposition). A soot blowing frequency of approximately once every 10 hours will be required to keep the ash layer thickness below 0.25 in. on the downstream tubes.

Based on these results, a staggered, elliptical tube, air heater design has been selected for further study. Conjugate heat transfer calculations will be performed to evaluate heat transfer performance and to determine material temperatures for input to a finite element stress analysis code.

AIR HEATER MATERIALS

Oxidation, corrosion, thermal conductivity, strength and fabricability are among the most important properties considered in the selection of heat exchanger and combustor materials. At present, the nickel base alloys rather than the ferrous alloys are the bulwark of high temperature metallurgical technology in gas turbines, furnaces and a myriad of highly specialized modern products.

The materials used for combustors and heat exchangers must exhibit fabricability. They must be weldable and formable. The current gas turbine combustor materials are typified by the nickel base alloy Hastelloy X and the cobalt base alloy Haynes 188. These alloys (superior to the ferrous base alloys typified by Incology 800) exhibit the necessary tensile strength, ductility creep rupture, low cycle fatigue, and creep fatigue interaction behavior. They also exhibit sufficient environmental resistance as well as resistance to thermal aging and embrittlement. Unfortunately the nominal upper metal operating temperature is 1600°F (870°C).

Wrought precipitation hardened nickel base alloys typified by Inconel 617, Incology 903A and Inconel 718 exhibit superior high temperature strength and improved environmental resistance, but are not readily available in sheet form. Moreover, the slight advantages they offer are offset by the poor resistance to high temperature fatigue.

Inco has developed a number of mechanically alloyed, oxide dispersion strengthened (ODS) superalloys for gas turbine applications. At present the only ODS sheet material is MA 956, which is commercially available in gages down to thickness of 0.01 in. and widths up to 24 in.

Pratt & Whitney (Henricks, 1984) examined the feasibility of employing an oxide dispersion hardened alloy to replace Hastelloy X. In that study it was concluded that the family of ODS materials can offer a +167°C (300°F) advantage in creep strength, and a +167°C (300°F) advantage on cyclic oxidation resistance . However, the family of ODS alloys did not offer any improvement in thermal fatigue, and unfortunately, although the alloy can be fusion welded, the weldments are relatively weak. They did not report however that segmentation is a promising combustor design approach to accommodate the limited thermal fatigue capability of ODS alloys.

Although the physical metallurgy of the high temperature superalloys is exceedingly complex and subtle, the relationships of properties to structure in these systems is certainly the most well known of all materials for use over the range 1200–2200°F (649–1204°C). This allows their use to extend to the highest temperatures of any competitive materials. The mechanical properties of the superalloys depend on the size and distribution of precipitated phases, distribution of carbide phases and precise control of grain size and grain boundary chemistry. The ideal heat exchanger material should be a ductile single phase solid solution strengthened alloy with exceptional resistance to oxidation and corrosion.

The base alloy for the nickel base superalloys is Ni–20Cr, whose oxidation behavior has been intensively studied over the decades. Chromium oxide, (Cr_2O_3) is the protective scale that forms on

many of the nickel base alloys and the majority of the high temperature ferrous alloys (speciality steels). However, at elevated temperatures, chromia is further oxidized to the volatile trioxide (CrO_3). At temperatures above 1650°F (900°C), the loss of chromia via CrO_3 formation is sufficient to limit the usefulness of chromia forming scales.

The growth rates for a number of candidate oxide scales for oxidation protection is shown in Figure 23. It is immediately apparent that alumina is the oxide of choice. The temperature dependency of the parabolic rate constants for oxidation of Ni–Al alloys is known and the conditions necessary for continuous alumina scale formation have been described by Pettit (1967). In the nickel base alloy system, a minimum of 5% aluminum is needed to prevent continuous NiO scale formation. In the ferrous system, the critical concentration is less than 4% aluminum.

Allegheny Ludlum has developed a new FeCrAl superalloy for use at high temperature. ALFA–IV® alloy is a ferritic stainless steel containing nominally 20% chromium, 5% aluminum, and small amounts of the rare–earth metals cerium and lanthanum. ALFA–IV alloy is exceptionally resistant to oxidation at high temperature under both continuous and cyclic thermal conditions. Although the alloy is relatively weak at elevated temperatures, it forms the desired alumina scale. The measured parabolic scaling constant at 2100°F (1149°C), is 3.6 x 10^{-12} g/cm^{4}sec in excellent agreement with the kinetic data for alumina formers as shown in Figure 22.

Table 4. ALFA IV Typical Composition

Element	wt %
Mn	0.35
P	0.025
Si	0.45
Cr	20.2 min
Al	5.1 min
C	0.02
Ce	0.02
La	~0.5 Ce

The physical and mechanical properties of the alloy are compared with those of the nickel base alloys and the cobalt base alloy HAYNES 188 in Figures 23 to 26.

Minor modifications may need to be made to the ALFA–IV alloy to insure that the alumina scale resists spallation and the corrosive attack of fused salts and oxides present in the high temperature hostile environment of the HITAF. At present, the alloy is extremely weak at elevated temperatures. Additional objectives of the alloy modification program are an increase creep strength and weldability of the alloy.

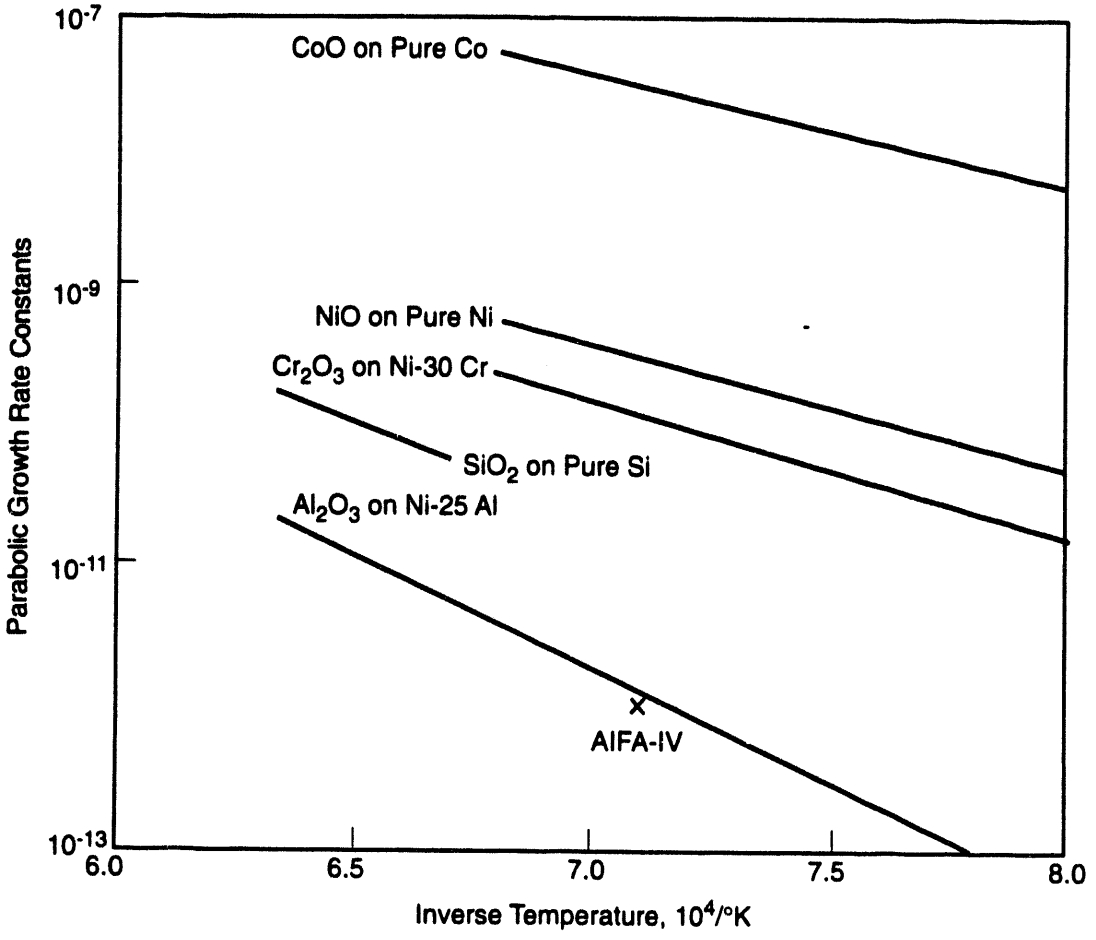

Figure 22. Growth rates of oxides.

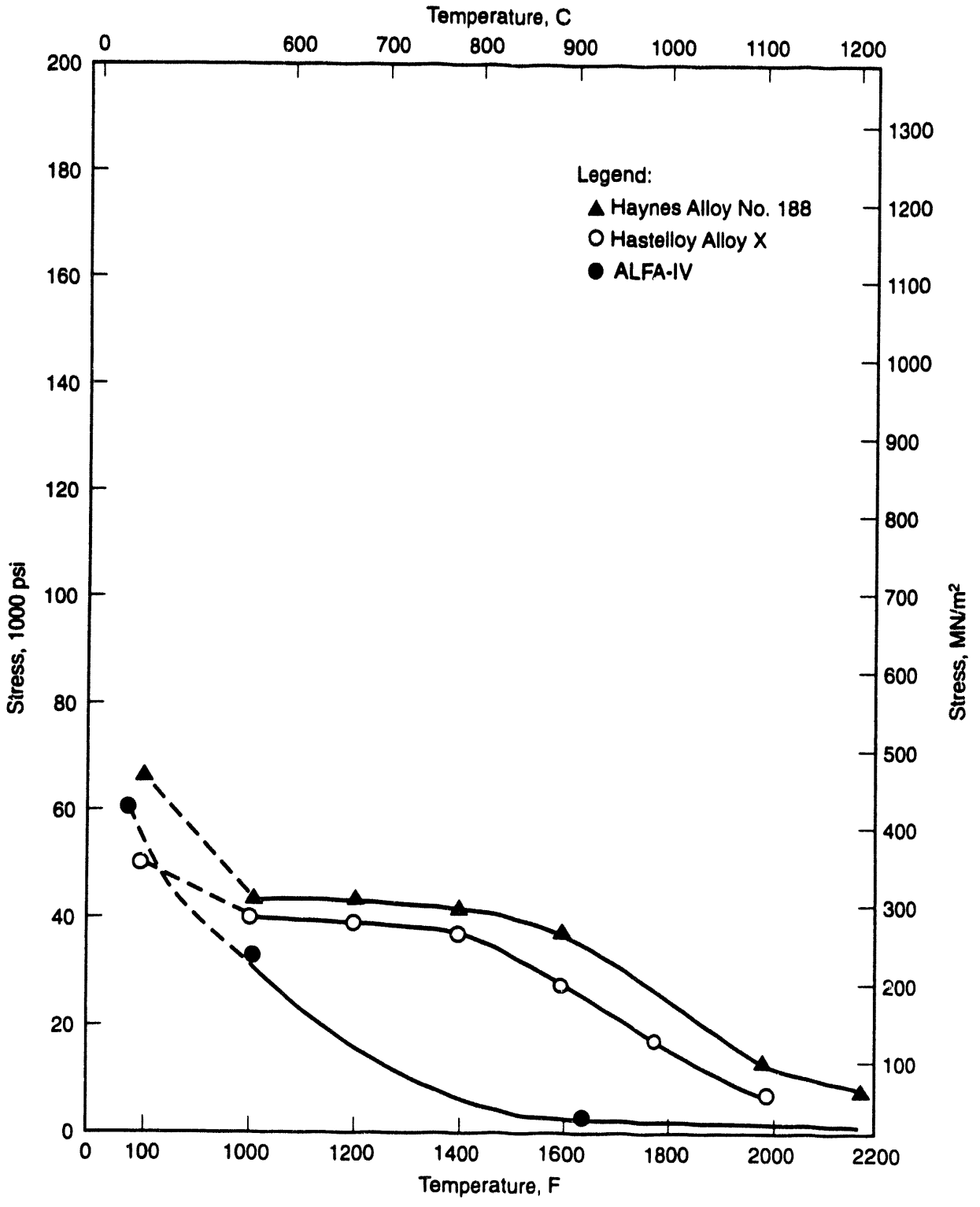

Figure 23. Sheet materials – yield strength (0.2% offset).

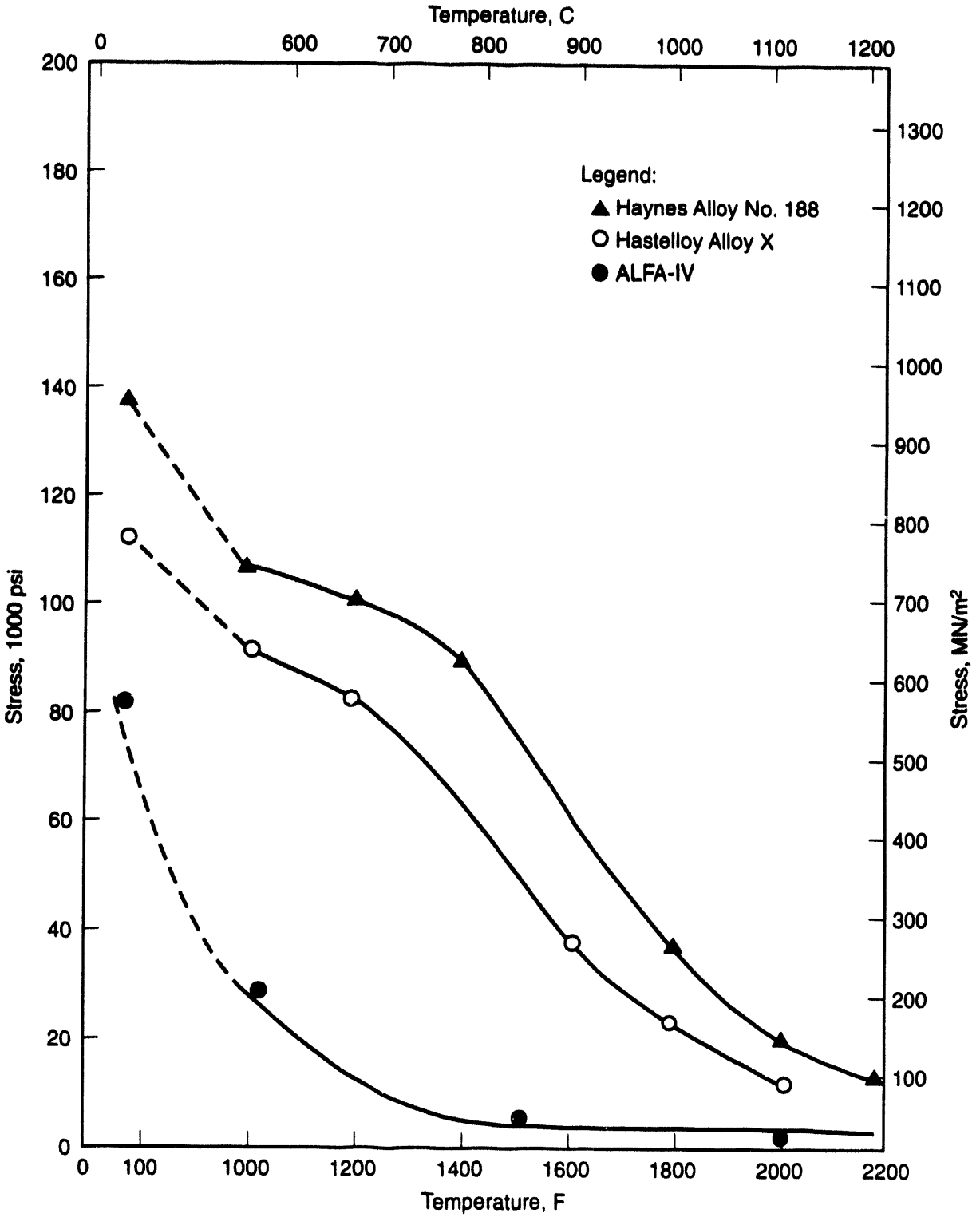

Figure 24. Sheet materials – ultimate tensile strength.

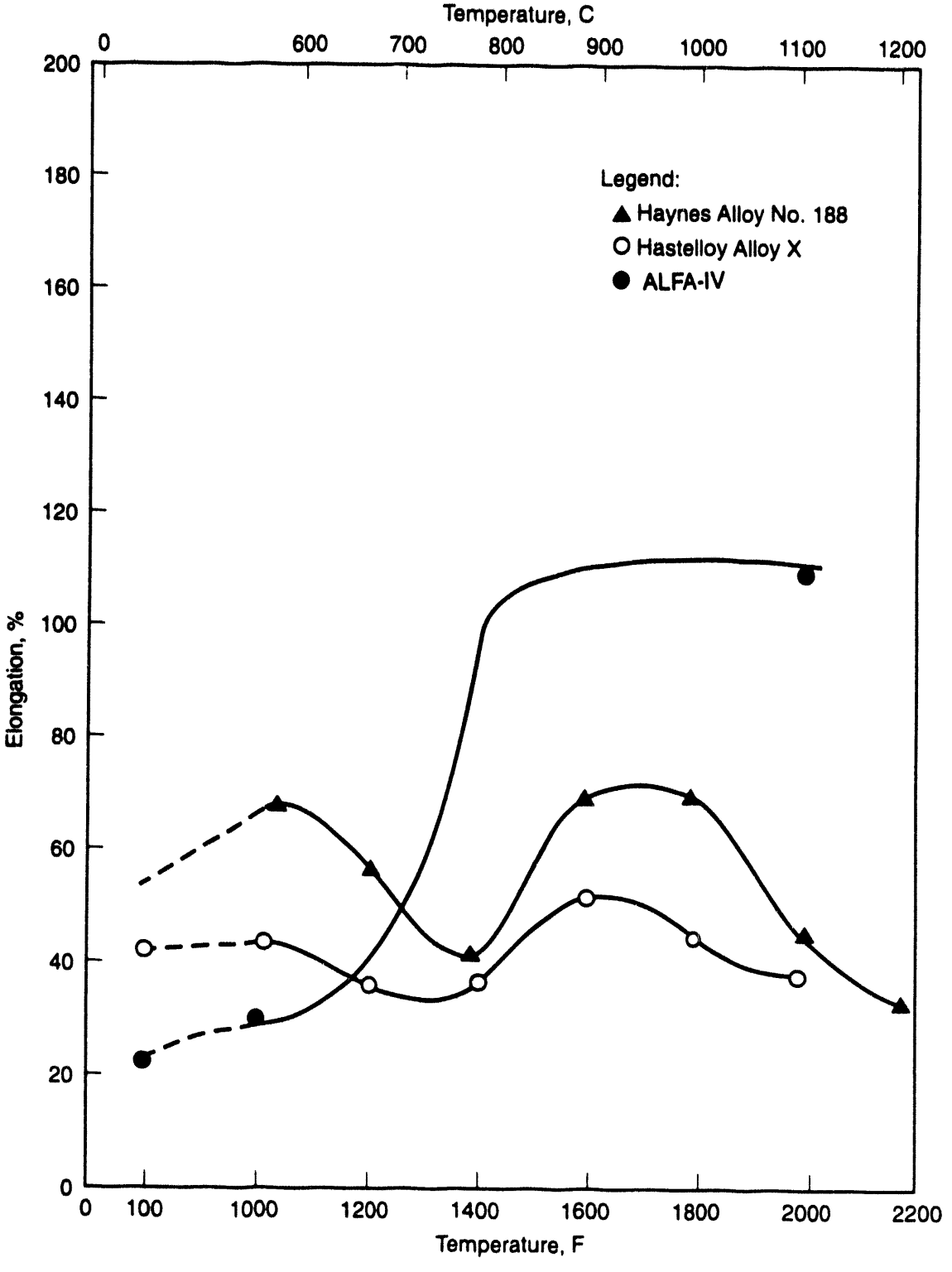

Figure 25. Sheet materials – tensile elongation.

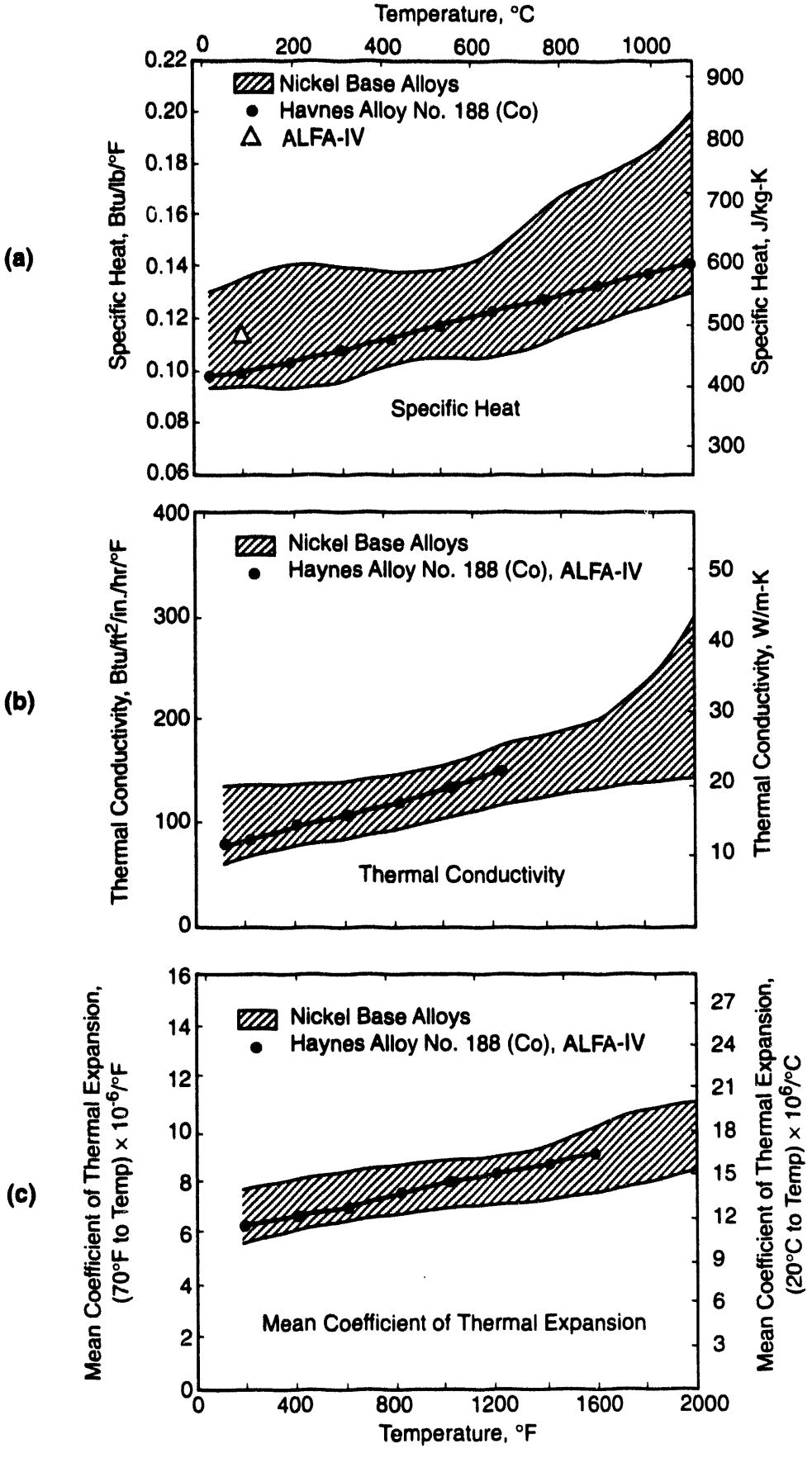

Figure 26. Physical properties.

DEPOSIT INITIATION AND GROWTH ON CERAMIC SURFACES

Refractory Experiments

In order to prevent slag corrosion of the ceramic air heaters in the high-temperature advanced furnace (HITAF), a replaceable coating of high-conductivity refractory will be applied to their surfaces. Previous tests of the corrosion resistance of commercially available silicon carbide-based monolithic refractories showed that nonmoving (static) Illinois No. 6 coal slag would penetrate one inch of refractory within five weeks. A high-calcium Powder River Basin coal slag was found to penetrate much more quickly. The primary corrosion mechanism for both slags was dissolution of the binder material. Therefore, we have spent much effort to find more corrosion-resistant binders.

Figure 27 shows a cross section of a cup made of commercially available monolithic silicon carbide (SiC) that was cured and fired to the manufacturer's specifications. This type of refractory, with a calcium aluminate-based binder, was previously found to be the most corrosion-resistant of the commercially available samples tested. After firing, the 1/2-inch diameter central cup was filled with ash from a Powder River Basin coal and reacted at 1450°C for 80 hours, then cut in half after cooling. The figure shows that much of the slag has flowed up and out of the cup, a problem always encountered with this type of slag. The flow occurs either because of excessive bubbling (caused by rapid SiC oxidation or slag decomposition) or because of extreme wetting of the refractory. The extreme wetting would indicate that the materials are likely miscible, so that corrosion would be rapid in flowing slag. The remaining slag is clear, indicating that it is amorphous and vesicular. The large number of bubbles in the glass indicates that oxygen was easily able to penetrate the remaining slag layer and oxidize the SiC, forming carbon dioxide that bubbled through the slag. No SiO_2 reaction layer is left at the surface of the SiC, indicating that it dissolved into the slag. The irregular interface between the slag and refractory shows corrosion through dissolution of the binder.

Figure 28 shows a cross section of a refractory cup made from SiC granules and an experimental binder designed for high calcium slags. The cup was filled with Powder River Basin coal slag and reacted at 1380°C for 80 hours. The binder was formulated to be a hydraulic cement to provide green strength to the refractory and then to fire to a composition with a solidus temperature of 1400°C (above the highest temperature expected to be reached by the refractory in the 65% coal scenario). The binder is formulated to raise the solidus temperature of the slag by approximately 150°C as it dissolves into the slag. In the 65% coal case, this increase should be enough to solidify a layer of slag next to the refractory as the binder dissolves, protecting the refractory from further corrosion.

As with the commercially available refractory, much of the slag had flowed out of the cup of refractory with experimental binder. As expected, some of the binder had dissolved into the slag, creating an irregular interface between the slag and the refractory, although the peak-to-valley distances were less than in the best commercially available refractory when corroded for half as long at a temperature 120°C lower. In addition, the remaining slag is white, indicating that it is crystalline.

Figure 27. Cross section of a cup made of commercially available monolithic SiC refractory filled with ash from a Powder River Basin coal and reacted at 1450°C for 80 hours.

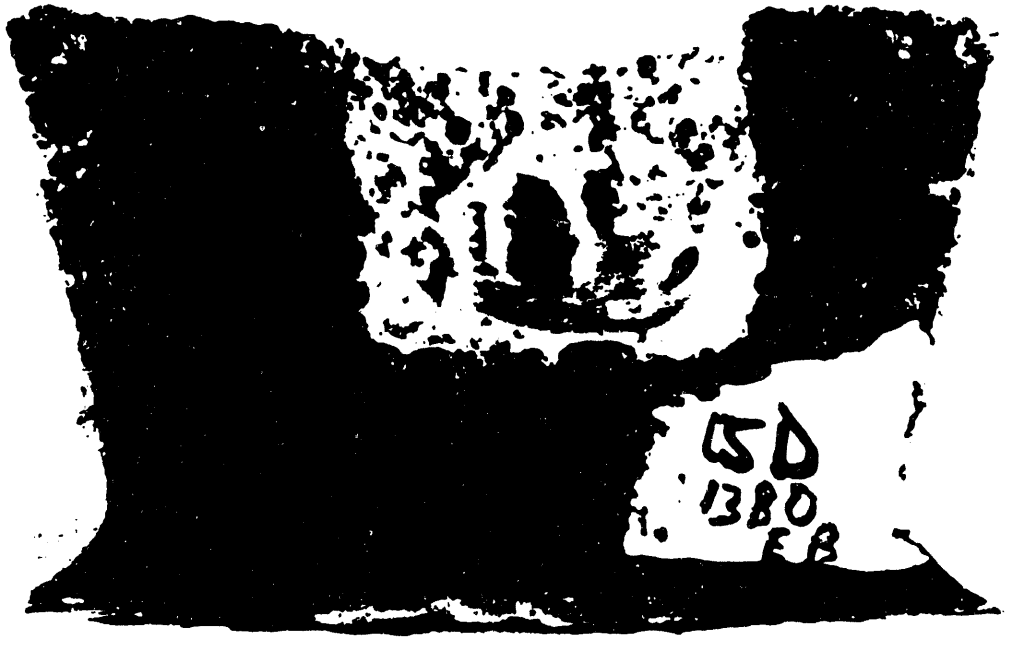

Figure 28. Cross section of a refractory cup made from SiC granules and an experimental binder designed for high–calcium slags. The cup was filled with Powder River Basin coal slag and reacted at 1380°C for 80 hours.

The composition of the slag remaining in the cup indicates that little of the binder dissolved into it, but the SiC did (probably oxidizing first). As was also true in tests of the commercially available refractories, the calcium content of the slag was depleted at the end of the test. Most likely a calcium-rich compound crystallized, but cannot be seen by backscatter electron imaging, indicating that if crystallization does occur, the crystals have the same average density as the rest of the slag. The solidus of the remaining slag is likely between 1135° and 1200°C, with a liquidus around 1500°C, indicating that crystallization is induced at much higher temperatures than in the original slag, but that liquid is still present, allowing the slag to flow. Also, the types of crystals that will form from the calcium-depleted slag are most likely soluble in unreacted slag, so protection from further corrosion is not likely with this particular refractory composition.

Figure 29 shows a cross section of another experimental refractory cup made from SiC and an experimental binder designed for low-calcium slags. The cup was filled with Illinois No. 6 coal slag and reacted at 1450°C for 80 hours. Penetration of slag into this refractory was also much lower than for commercial refractories treated similarly. Figure 30 gives the penetration rates of Illinois No. 6 coal slag for the best type of commercial refractory and refractories with 5%, 7.5%, and 10% experimental binder. The much slower rates of penetration show that the experimental refractories will last more than 10 times longer under similar conditions than the best available commercial monolithic SiC-based refractory.

In addition to greater corrosion resistance, the experimental refractory has a much greater thermoconductivity than commercially available materials. Figure 31 shows the temperature-dependent conductivity of experimental SiC-based monolithic refractory made with 15% binder. The drop and leveling of conductivity with increased temperature is common for dense SiC, although the conductivity of the dense materials usually drops linearly by another one third as the temperature rises to 1200°C. A linear extension of the conductivity of the experimental material shows no drop, possibly because the conductivity of the binder tends to rise with temperature. Even if the conductivity does drop by one third, the experimental material will have three times the conductivity of commercial material at 1200°C (a common temperature for conductivity measurements).

The combination of high conductivity, high corrosion resistance, and the probability of a coefficient of thermal expansion similar to that of dense SiC makes the experimental refractory ideal for protection of the radiant air heater in the HITAF. The material could be cast onto the panels while they lay prone; then, after curing, they could be hoisted into place in the HITAF and fired. The HITAF could be shut down twice a year for maintenance, during which time the refractory would be applied in a trowelable form to any excessively corroded areas. A large refractory manufacturer has been contacted who is willing to prepare appropriate batches and to work with us to improve the refractory during Phase 2 of Combustion 2000.

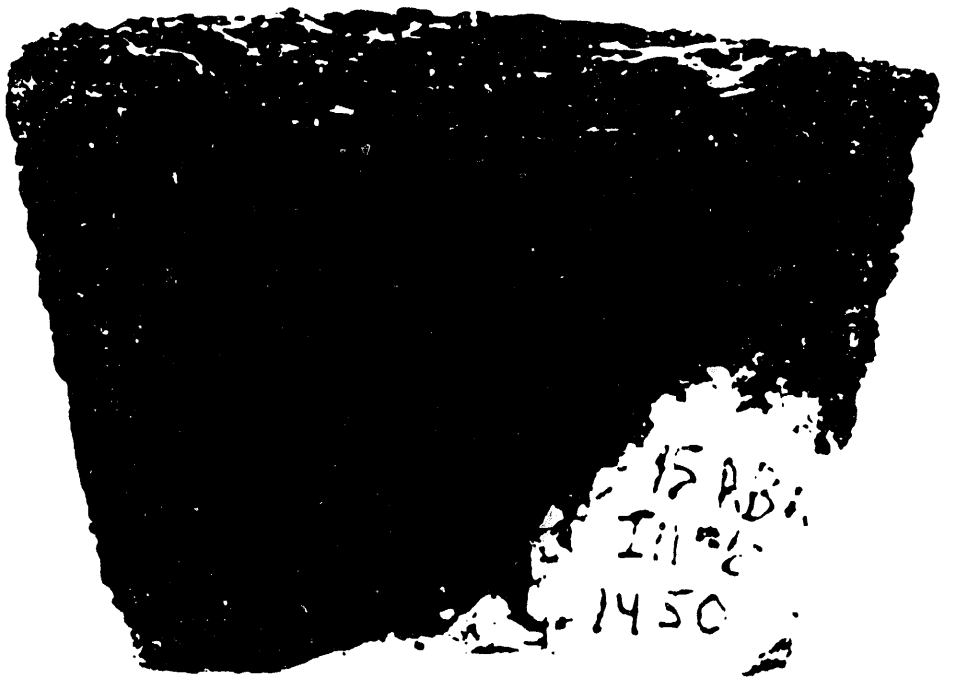

Figure 29. Cross section of experimental refractory cup made from SiC and an experimental binder designed for low–calcium slags. The cup was filled with Illinois No. 6 coal slag and reacted at 1450°C for 80 hours.

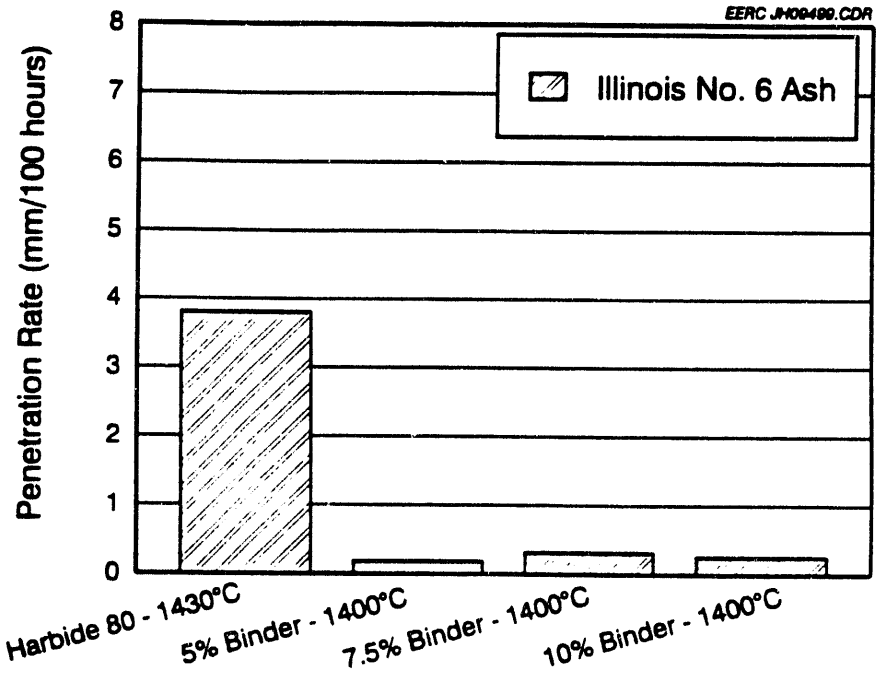

Figure 30. The penetration rates of Illinois No. 6 coal slag for the best type of commercial refractory and refractories with 5%, 7.5%, and 10% experimental binder.

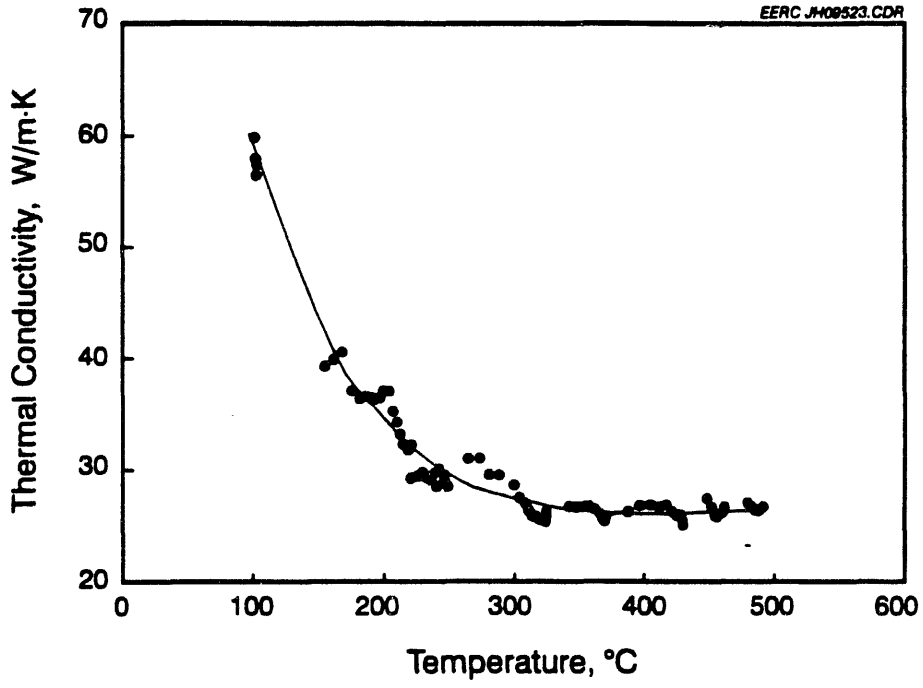

Figure 31. The temperature–dependent conductivity of experimental SiC–based monolithic refractory made with 15% binder.

Ceramic Sting Tests – Results for the Experimental DIMOX at 1260°C

The 300–hour sting tests at 1090°C and 1260°C were completed in May and June using four different ceramic materials, which included Hexoloy sintered alpha SiC (carborundum), NT230 siliconized SiC (Norton), standard DIMOX SiC–Al_2O_3–AlSi composite (Lanxide), and an experimental DIMOX SiC–Al_2O_3 composite. The ceramics were exposed to the Wyodak and the Illinois No. 6 ashes, which were produced by burning pulverized fuel in a drop–tube furnace. The results of chemical analyses of the ashes are given in Table 5. Only the results from the 1260°C sting test for the experimental DIMOX SiC–Al_2O_3 composite samples will be reported here. The other samples are in the process of being analyzed, and those results will be reported in the October through December quarterly report.

The experimental DIMOX composite contained approximately 40% SiC, 50% Al_2O_3 (alumina), and 10% residual AlSi alloy. According to Lanxide, the experimental material contains less residual aluminum than the standard DIMOX. The experimental material also is not preoxidized, whereas the standard material is oxidized to form an alumina coating on the composite surface.

Table 5. XRF Analyses for Ashes Used in Corrosion Experiments

Sample	Wyodak	Illinois No. 6
Oxide, wt%		
Na_2O	1.0	0.4
MgO	7.7	0.9
Al_2O_3	18.6	20.0
SiO_2	38.7	51.2
P_2O_5	1.2	0.0
SO_3	0.3	0.9
K_2O	0.2	1.9
CaO	25.2	5.5
TiO_2	1.3	0.9
Fe_2O_3	5.8	18.4

Experimental

Machined blocks of the experimental DIMOX measuring 50 x 44 x 3 mm were used for the tests so that ten 50 x 4 x 3–mm flexure test bars could be cut from each. The samples were embedded in the bottom of a castable SiC refractory boat that contained the coal slag during the exposure (Figure 32). Approximately 6.0 grams of ash were packed onto the surface of the samples and placed in an atmospheric muffle furnace. The furnace temperature was raised to 1260°C at the rate of 120°C/hr, and the samples were exposed for 300 hours. Then, the samples were cooled at a rate of 120°C/hr to ambient temperature. The experimental DIMOX samples were cracked after the exposure. The

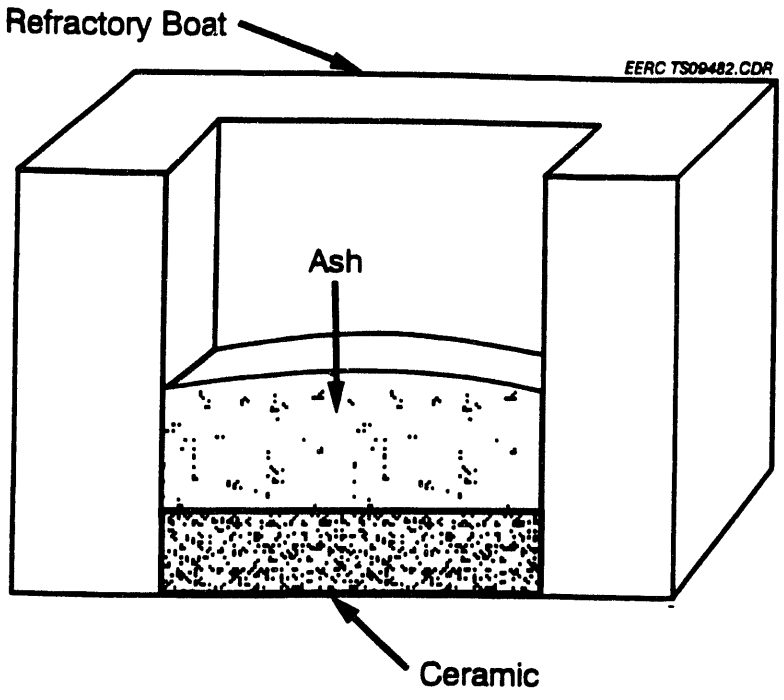

Figure 32. Illustration of the composite sample embedded in a refractory boat. The refractory boat design allowed containment of the slag during the exposure and prevented interaction of the base of the composite with the slag or refractory.

cracking probably occurred during the cooling of the furnace, because no slag infiltration was observed that would have indicated cracking during the exposure. The cracking may be a result of a thermal expansion mismatch between the refractory and the composite. The samples were cross-sectioned to expose the ceramic–ash interfaces, which were examined using scanning electron microscopy with energy-dispersive x-ray analysis (SEM–EDX).

Results

Results for the Wyodak Ash

A highly vesicular, tan-colored slag was present on the surface of the ceramic sample. The slag layer thickness was 600–800 μm. The slag vesicles ranged in size from 100 to 1000 μm in diameter, with the smallest vesicles present at the slag–ceramic interface. SEM analyses revealed that the slag was depleted in calcium and enriched in silicon relative to the original ash. The calcium depletion can be explained by the presence of crystals with an anorthitelike composition ($CaAl_2Si_2O_8$) (Figure 33). The enrichment in silicon could be a result of the degradation of the SiC portion of the composite or degradation of the SiC refractory boat. There was evidence that the refractory boat reacted with the slag during the exposure.

Figure 33. SEM backscatter electron image of a cross section through the composite showing anorthitelike crystals in the slag and a dark alumina scale present at the slag–ceramic interface.

The surface of the ceramic was coated with a continuous, 10–μm–thick alumina–rich layer visible in the x–ray map of aluminum (Figure 29). The alumina–rich layer is coated with a thicker (25 μm), continuous reaction layer composed of anorthitelike crystals. The layer shows up in the silicon x–ray map as the dark grey layer on the surface of the ceramic because silicon is depleted in the anorthitelike layer (Figure 34). The top portion of the anorthitelike layer contains isolated, calcium–magnesium–rich crystals with a composition like augite [$(Ca,Na)(Mg,Fe,Al)(Si,Al)_2O_6$], which are the bright white phases, approximately 10 μm across, with a prismatic morphology.

The formation of an alumina scale on SiC–Al_2O_3 composites has been documented in other corrosion studies (Kern et al., 1992). This oxide scale can form as a result of the oxidation of the residual aluminum metal exuded from the material during high–temperature exposure. The formation of the alumina scale on the composite could have occurred during the prefiring of the refractory material or during the manufacture of the composite.

There are a large number of pores near the surface of this sample, which indicate that aluminum was exuded from the composite (Figure 35). When the exuded aluminum reaches the surface, it oxidizes and forms an alumina scale. If the alumina scale forms a continuous cohesive layer, then the increased surface porosity of the composite may not affect corrosion. But if the alumina scale is

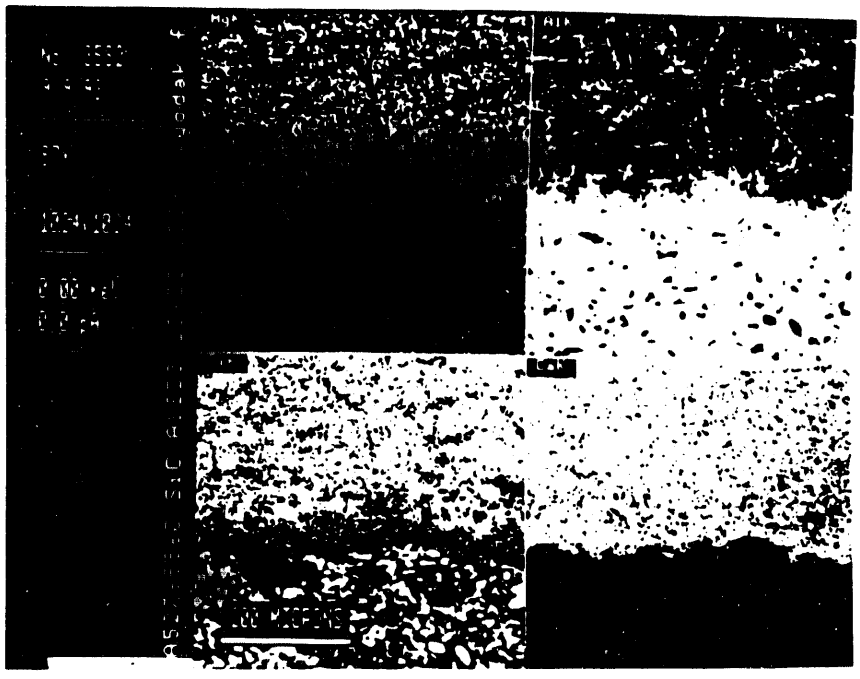

Figure 34. X-ray map of Figure 28 showing a layer rich in Al at the slag-ceramic interface, and a layer rich in Si and Al, composed of anorthitelike crystals, on the alumina scale.

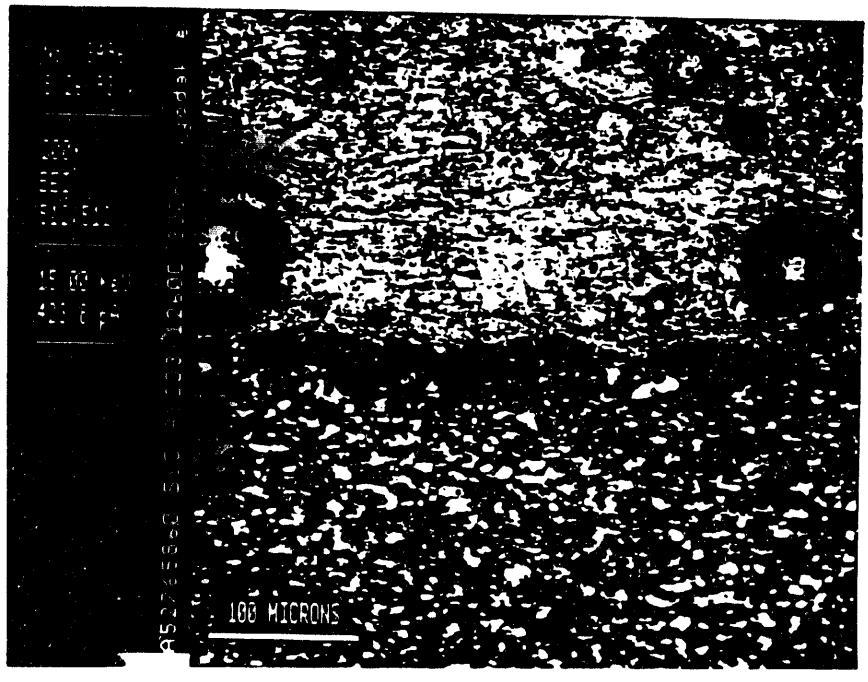

Figure 35. SEM photo showing porosity development on the surface of the composite. The pores are black and concentrated along the slag-composite interface in the center of the photo.

removed by reaction or spalling, then the increased surface porosity might increase the rate of corrosion.

In summary, the calcium and silicon in the coal slag reacted with the surface of the alumina scale to form the anorthitelike reaction layer and the augitelike crystals. The slag attack on the ceramic was limited by the presence of the alumina scale acting as a barrier to the reaction of the slag with the composite surface. During the alumina scale formation, some porosity developed on the ceramic surface.

Results for the Illinois No. 6 Ash

A highly vesicular black slag, containing vesicles ranging in size from 100 to 1000 μm in diameter, was present on the ceramic surface after the experiment. The slag was depleted in iron and enriched in silicon relative to the original ash. The silicon enrichment could be a result of reaction with the composite or with the SiC refractory. The slag also contained several crystalline phases with compositions indicating they were mullite ($3Al_2O_3 \cdot 2SiO_2$) and cristobalite (SiO_2). Some iron substitution was present in the mullite crystals and may account for the iron depletion in the slag.

The slag–ceramic interface was undulating, and a thin (<20 μm), alumina–rich scale was present on the ceramic surface, similar to the scale found on the ceramic exposed to the Wyodak ash (Figure 36). A 25–μm–thick reaction layer containing aluminum, silicon, and iron was present on top of the alumina scale (Figure 37). This reaction layer was similar in composition to mullite, substituting iron for aluminum, and had the same appearance as the mullite crystals in the slag. Small, isolated crystals rich in iron, aluminum, and silicon ($Fe_3Al_2Si_3O_{12}$), similar in composition to iron–rich garnets, were present along the top edge of the mullite reaction layer.

As with the ceramic exposed to the Wyodak ash, the formation of the alumina scale may have prevented or slowed corrosion of the composite material. The melting point of pure alumina is approximately 2000°C; therefore, the alumina scale is stable at 1260°C. The scale also appears dense as compared to the SiC–Al_2O_3 composite, which would limit diffusion of ions through its structure. The SiC–Al_2O_3 composite developed porosity near the surface because of aluminum metal exuded during the exposure. Again, this may cause corrosion problems if the alumina scale becomes detached. In this experiment, the alumina scale formed a cohesive layer which acted as a barrier to the slag.

Conclusions

The corrosion resistance of SiC–Al_2O_3 composites by coal slags is enhanced by the formation of an alumina–rich scale on the ceramic surface. This scale probably forms as a result of the oxidation of residual aluminum metal that has migrated to the ceramic surface (Kern et al., 1992). The alumina scales that formed on the surfaces of the SiC–Al_2O_3 composite in these experiments impeded the slag corrosion of the composite.

The rate of formation of the alumina scale is controlled by the rate of transport of aluminum to the surface, and not by the diffusion of oxygen to the aluminum, since no residual metal was left at the

Figure 36. SEM photo of a cross section through the composite showing the dark alumina scale and the overlying, lighter layer of mullite crystals above the slag–ceramic interface. The mullite layer is coated with small, bright crystals of almandine.

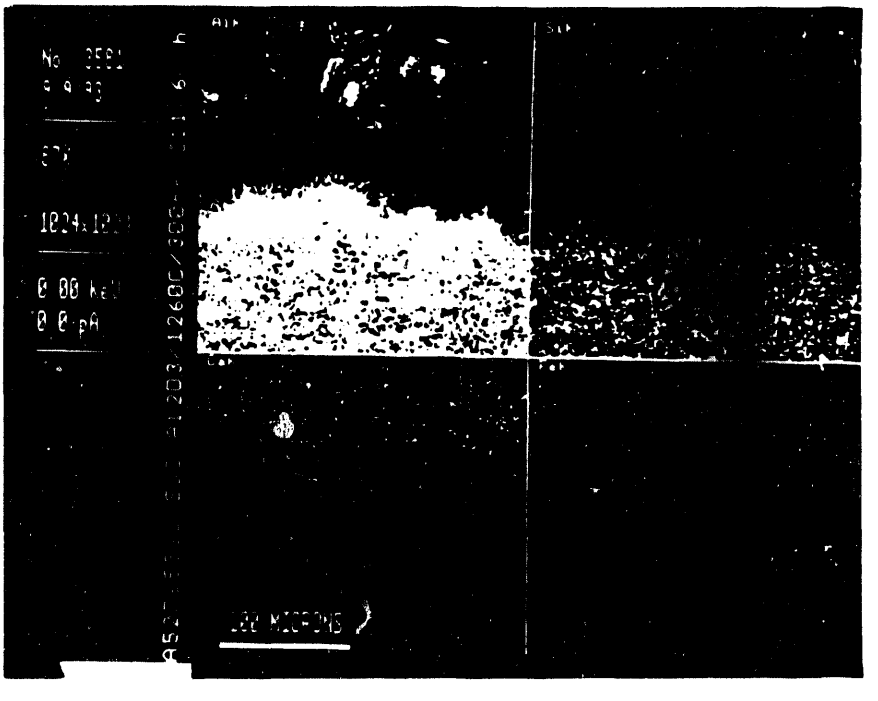

Figure 37. X–ray map of Figure 31 showing the concentration of Al, Si, Fe, and O_2 in the mullite reaction layer at the slag–ceramic interface.

surface. The migration of residual metal from the bulk material leaves pores near the surface of the composite (Nowok, 1982). This is evident in the SEM micrograph of the sample exposed to the Wyodak ash (Figure 35). The rate of transport of the aluminum to the surface depends upon the degree of wetting of the SiC matrix by the aluminum and upon the surface area and tortuosity of the remaining pores and would decrease with time. The rate of loss of the alumina by a flowing slag would be constant, so that the surface of the alumina would recede linearly with time. Therefore, at some time in the future, the rate of alumina scale formation would fall below the rate of dissolution, and the scale would be dissolved. The loss of the scale would leave the porous remaining SiC structure open to direct slag attack. However, without flowing slag tests, it is not possible to predict the time required for loss of the alumina scale. In addition, the increased surface porosity may become a concern if the alumina scale and composite material have incompatible coefficients of thermal expansion (CTE). The material used in these experiments contained approximately 50% SiC, resulting in a CTE similar to that of the alumina scale.

The stability of the alumina scale is an important factor in determining the corrosion resistance of the SiC–Al_2O_3 composite. Future research efforts should focus on the effects of temperature and coal slag composition on the stability of the alumina scale and on corrosion rates when no scale is present.

Slag Additives – Copper Oxide

A literature survey on the effects of copper oxychloride additions on slag behavior was reported in the April through June quarterly technical progress report. A laboratory experiment was conducted to determine the effects of copper oxide (CuO) additions on crystallization of a high–iron Illinois No. 6 slag. A small addition of CuO (1 wt.%) was added to the ash. The ash and copper mixture was heated to 1400°C for 30 minutes then quenched. The slag was examined with SEM–EDX.

The SEM revealed a high concentration of small (< 5μm) blocky crystals in the slag as shown in Figure 38. Analyses indicated that iron and oxygen were the main elements present in the crystals, which are probably magnetite (Fe_3O_4). The formation of these crystals may influence the slag corrosion of SiC ceramics in several ways. The formation of crystals can increase slag viscosity by increasing frictional forces in the slag. Also, magnetite formation would reduce the amount of iron in the residual slag, which would increase the viscosity of the residual melt if the iron were present in the ferrous state (ferrous iron is primarily present at temperatures over 1500°C or when oxygen concentrations are low, as is expected near the upper wall of the HITAF). The higher viscosity of the slag would slow its flow and decrease its velocity, thereby decreasing its erosiveness. The formation of the crystals ties up the iron, a major player in SiC corrosion, in a phase which may be more stable than the iron silicide formed during corrosion of the SiC, thus eliminating the contribution of iron to SiC corrosion.

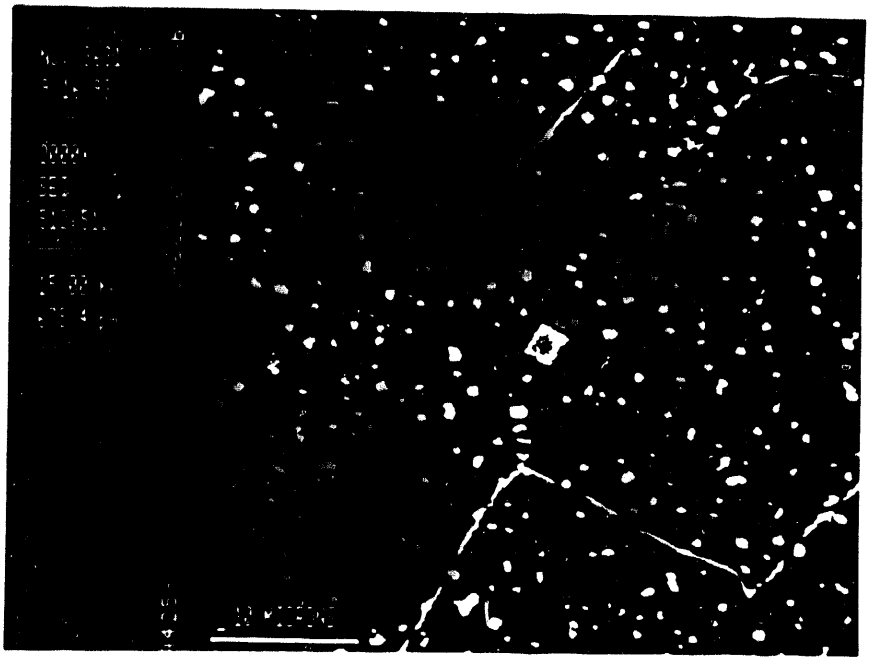

Figure 38. SEM photo showing iron oxide crystals that formed in the Illinois No. 6 slag with a 1 wt% copper oxide addition.

REFERENCES

Heap, M.P. and B.A. Folsom (1990), "Optimization of Burner/Combustion Chamber Design to Minimize NOx Formation During Pulverized Coal Combustion," Ch. 10, Pulverized Coal Combustion: Pollutant Formation and Control, 1970–1980, EPA–600/8–90–049.

Henricks, R. and K. Sheffler (1984), "Materials for Advanced Turbine Engines (MATE)," NASA CR–174691.

Kern, W.A.; R. E. Tressler; and M. J. McNallan (1992), "Durability of SiC/Al_2O_3 Composites in Contact with Sodium Silicate," *Center for Advanced Materials Newsletter, 6* (1), 1–6.

Michels, J. and R. Payne (1988), "Detailed Measurement of Long Pulverized Coal Flames for the Characterization of Pollutant Formation," Part II, Fundamental Combustion Research Applied to Pollutant Formation, Volume IIa. Physics and Chemistry of Two–Phase Systems: Flame Combustion Processes, EPA–600/7–88–001a.

Nowok, J. (1982), "Formation Mechanisms of Keying or Pegging Yttrium Oxide and Increased Plasticity of Alumina Scale of FeCrAlY," *Oxidation of Metals, 18*, 1–17.

Pershing, D.W., M. P. Heap and S. L. Chen (1990), "Bench–Scale Experiments on the Formation and Control of NOx Emissions from Pulverized Coal–Combustion," Ch. 9, Pulverized Coal Combustion: Pollutant Formation and Control, 1970–1980, EPA–600/8–90–049.

Petit, F. (1967), Trans. TMS–AIME, 238, 1296.

DATE

FILMED

4/19/94

END